



Research Article

Analysis of a Single-Phase Grid-Tied Photovoltaic Inverter for Enhanced Performance Using TLBO-HHOA Regulated FOTDAF Controller

Debswarup Rath^{a*}, Akshaya Kumar Patra^b, Sanjeeb Kumar Kar^a

^a Department of Electrical Engineering, ITER, Siksha 'O'Anusandhan University, P. O. Box: 751030, Bhubaneswar, Odisha, India.

^b Department of Electrical and Electronics Engineering, ITER, Siksha 'O'Anusandhan University, P. O. Box: 751030, Bhubaneswar, Odisha, India.

PAPER INFO

Paper history:

Received: 20 December 2022

Revised: 05 March 2023

Accepted: 12 July 2023

Keywords:

TLBO-HHOA Regulated FOTDAF, IFOBC, Robustness, RSMI, SVPWM

ABSTRACT

The primary objective of the proposed work is the design of a Hybrid Teaching Learning-based Horse Herd Optimization Algorithm regulated Fractional Order Tilt Derivative Acceleration with Filter (TLBO-HHOA regulated FOTDAF) controller for enhanced performance and enhanced devaluation of harmonic components of the grid-connected photovoltaic system. The solar photovoltaic system incorporates constituents such as a photovoltaic array, interleaved fractional order boost converter (IFOBC), Reduced Switch Multilevel Inverter (RSMI), and TLBO-HHOA regulated FOTDAF controller. IFOBC is preferred over boost converter because of its low ripple voltage, faster transient response, high efficiency, low duty cycle, reduced EMC, and improved reliability and stability. In this control strategy, the control logic is formulated by using a Tilt Integral Derivative Controller (TIDC), whose control parameters are considered as a function of the error to improve the robustness. The validation, better performance, and superiority of TLBO-HHOA regulated FOTDAF are established by comparative result analysis using modern controllers. This study implements TLBO-HHOA-regulated FOTDAF and applies Support Vector Pulse Width Modulation (SVPWM) technique. The proposed model managed to achieve improvements in overall system response and reduced harmonic distortions as well as better accuracy, improved stability, improved robustness, and better capabilities to handle system uncertainties.

<https://doi.org/10.30501/jree.2023.377522.1521>

1. INTRODUCTION

The major components of the proposed photovoltaic system include a photovoltaic array, a boost converter, an RSMI, and a TLBO-HHOA-regulated FOTDAF. The Interleaved Fractional Order Boost Converter (IFOBC) is the technique used for boosting voltage. IFOBC employs two switches (one controlled and one uncontrolled). Control switching is achieved through an Insulated Gate Bipolar Transistor (IGBT) while the diode is used for uncontrolled switch (Fang et al., 2020; Xie et al., 2020; Jia et al., 2018; Ayop et al., 2018). Switching for IFOBC is achieved using the TLBO-HHOA regulated FOTDAF controller. A gating signal for the controlled switches is generated by such techniques as Second-order Generalized Integrators based Phase Locked Loops (SOGI-PLL) (Xu et al., 2019), Artificial Neural Network (ANN) (Palanisamy et al., 2020), Proportional Resonant Controller (PRC) (Keddar et al., 2019; Sattianadan et al., 2020), Artificial Neuro-Fuzzy Interface System (ANFIS) (Logeswaran et al., 2015), Hysteresis Control (HC) (Guohua et al., 2022), Digital Signal Processing based controller (DSP) (Nguyen et al., 2022; Lin et al., 2020), Proportional Integral Derivative

Controller (PIDC) (Rath et al., 2021), among others. The advantages of a control system along with fractional theory-based calculus are combined to form the TLBO-HHOA-regulated FOTDAF (Tufenkci et al., 2020; Yao et al., 2021; Eberlein, et al., 2021). TLBO-HHOA-regulated FOTDAF combines the benefits of fractional-order calculus and control theory. The proposed control technique is very efficient in mitigating noise and disturbances while improving steady-state performances. TLBO-HHOA-regulated FOTDAF shares its structure with TIDC (Patra et al., 2020; Patra et al., 2021). The disparity in research concerning the TIDC design results from longer simulation time, longer settling time, and lower noise rejection ability, which limited its use. The research gap is addressed by replacing the integral block in TIDC with an accelerative component and variation of control parameters as a function of error. The application of the accelerative component enhances stability, robustness, steady-state response, faster response to noise signal mitigation, and noise rejection ability while the variation of control parameters as a function of error enhances the robustness of the photovoltaic system. The benefits of control theory, fractional calculus, and variation of control parameters have never been combined before. Thus, drawing inspiration from the concepts mentioned above, a new control technique (TLBO-HHOA regulated FOTDAF) is proposed for the solar photovoltaic system. The control parameters of the TLBO-

Corresponding Author's Email: debswaruprath@gmail.com (A. Kumar Patra)
URL: https://www.jree.ir/article_178968.html

Please cite this article as: Rath, D., Kumar Patra, A. & Kar, S. K. (2024). Analysis of a Single-Phase Grid-Tied Photovoltaic Inverter for Enhanced Performance Using TLBO-HHOA Regulated FOTDAF Controller, *Journal of Renewable Energy and Environment (JREE)*, 11(1), 46-64. <https://doi.org/10.30501/jree.2023.377522.1521>.



HHOA regulated FOTDAF are tuned using optimization technique (TLBO-HHOA) to ensure a better response (Lakshmi et al., 2021). This optimization technique hybridizes the TLBO algorithm and WOA. The superiority of TLBO-HHOA over other optimization techniques derives from its easier implementation, high convergence power, and ability to avoid being trapped at local optima. The superiority of the used optimization technique is validated by performing a comparative analysis with other optimization techniques (Izci et al., 2022; Eker et al., 2021; Izci et al., 2022; Izci et al., 2022). The 15-level Reduced Switch Multilevel Inverter (RSMI) receives the Direct Current (DC) voltage from IFOBC. Multilevel inverter topologies play a crucial role in applications that require medium voltage. Several reduced switch MLI topologies have been developed for various applications such as drives, electric vehicles, and renewable energy sources. These reduced switch MLI topologies offer several advantages compared to traditional two-level inverters, including a reduced number of switches, lower switching losses, cost-effectiveness, high-resolution output voltage, and ease of control. These features make them particularly suitable for low-power applications. This study examines a 15-level multi-level inverter with a reduced switch configuration for solar photovoltaic systems. When compared to the flying capacitor multi-level inverter, the cascaded type multi-level inverter, and the diode clamped multi-level inverter, the proposed method stands out by utilizing the minimum number of switches while achieving the maximum number of steps in generating staircase AC output voltage. The cost of the system is reduced by using the smallest number of switches possible. In this topology, a square wave switch is used instead of pulse width modulation to eliminate switching losses. As a result, the harmonics and total harmonic distortion (THD) in the pulsating AC output voltage waveform are reduced (Sampaio et al., 2022; Yusof et al., 2022; Liu et al., 2022; Karimi et al., 2019; Darmawardana et al., 2019; Fani et al., 2019; Alluhaybi et al., 2019). The primary benefit of using an RSMI is its ability to reduce voltage stress on the components, abdicates the use of transformers, facilitates improving Electro Magnetic Compatibility (EMC) of the proposed system, and helps reducing Total Harmonic Distortion (THD) (Siddique et al., 2019; Fahad et al., 2021). The controlled switches present in the 15-level RSMI are triggered by the use of the SVPWM technique (Yao et al., 2021). The standard for measuring Total

Harmonic Distortions (THD) present in a current signal is provided by IEEE-519 (Marrero et al., 2022). The novelties of the proposed work are enhanced robustness, accuracy and stability, better harmonic and disturbance suppression ability, and improved competence to handle uncertainties. The significant contributions associated with the TLBO-HHOA-regulated FOTDAF-based photovoltaic systems are listed below.

- Design of a single-phase photovoltaic model in a simulation-based software environment for performance analysis.
- Formulation of a control strategy (TLBO-HHOA regulated FOTDAF) using SVPWM for the photovoltaic system to ensure superior performance and enhanced harmonic devaluation.
- Justification of superior performance assessment of harmonic distortions in the case of the proposed photovoltaic system.
- Enhancement of robustness and noise reduction ability of the TLBO-HHOA regulated FOTDAF-based photovoltaic system.
- The validation of the superior performance of the TLBO-HHOA-regulated FOTDAF-based photovoltaic system is carried out by performing a relative exploration with prevalent practices.

The remaining sections of this study are organized as follows. Section 2 provides the mathematical modeling of the photovoltaic cell, IFOBC, 15-level RSMI, and SVPWM, along with an open-loop analysis of the proposed photovoltaic system. Section 3 examines the mathematical modeling of the proposed control technique (TLBO-HHOA regulated FOTDAF) and its ability to reject disturbances. Section 4 discusses the analysis results and validates the enhanced performance and robustness. Finally, Section 5 presents the concluding remarks.

2. PROBLEM FORMULATIONS

The major components of the proposed photovoltaic system are RSMLI, photovoltaic cell, DQC-SPWM, triggering mechanisms, TLBO-HHOA-regulated FOTDAF, and IFOBC. Figure 1 depicts the framework for the proposed photovoltaic system. The appending subsections present the extensive modeling of the photovoltaic system.

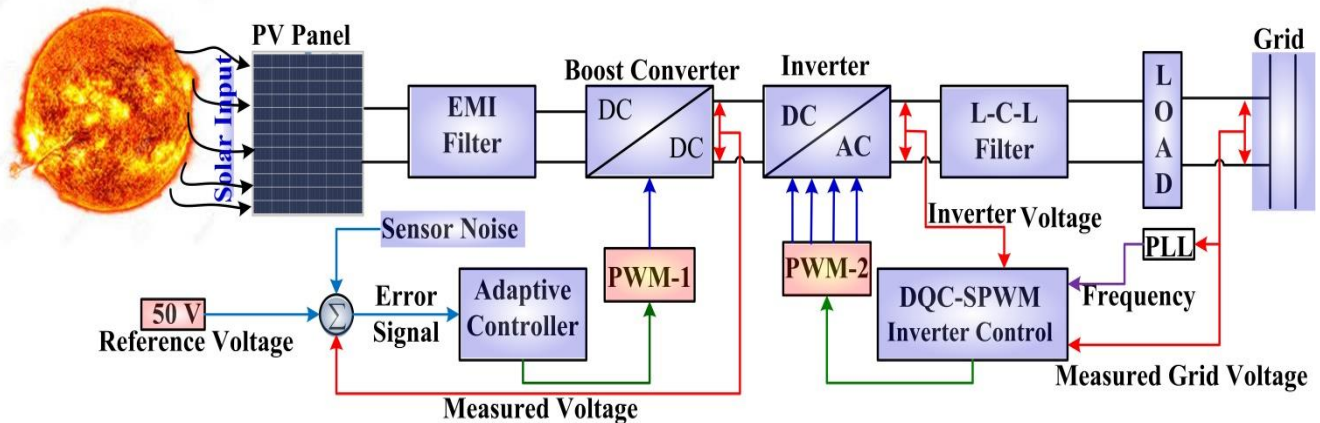


Figure 1. Schematic representation of the closed-loop photovoltaic system.

2.1. Photovoltaic system

Photovoltaic systems are classified based on their operating modes. They exhibit capabilities to operate under unaided and grid-tied modes. In the unaided mode, the photovoltaic system supplies the load alone. However, in the grid-tied mode, the power rating of the load is shared by both grid and photovoltaic systems. Of note, both grid and photovoltaic systems have the ability to feed the load singly. The proposed photovoltaic system operates in the grid-tied mode due to its better penetration in the single-phase networks, low maintenance charges, low electricity consumption from the grid, easy installation, short gestation period, not requiring additional storage facilities, and reliability. The photovoltaic system consists of such components as a photovoltaic array, IFOBC, TLBO-HHOA regulated FOTDAF, RSMI, SVPWM, and an electromagnetic filter. The inputs to the photovoltaic array include irradiance and temperature. The voltage induced in the photovoltaic array is of low magnitude and cannot be used directly. Hence, the IFOBC facilitates stepping up and fixing the voltage irrespective of the solar inputs. The ratings of the photovoltaic array are given in Table 1. The switches in the boost converter are switched by the proposed control technique. This research adapts to a fractional-order controller for efficient modeling and switching of the boost converter. The voltage from the boost converter is fed to RSMI. The IGBTs present in RSMI are triggered by the SVPWM technique. The electromagnetic filter is connected to the solar panels to reduce disturbance and suppress electromagnetic noise.

Table 1. Solar panel specifications.

Criterion	Values
Maximum power	60 watt
Voltage at maximum power	33.54 volts
Current at maximum power	1.89 ampere
Open-circuit voltage	39.66 volts
Short-circuit current	1.99 ampere

2.2. Boost converter

The advantages of interleaving are low ripple voltage, faster transient response, high efficiency, low duty cycle, reduced EMC, and improved reliability and stability. The application of fractional-order theory provides an extra degree of freedom and flexibility in the circuit design. The IFOBC is modeled using the model averaging technique for studying the dynamical response of IFOBC (Fang et al., 2020; Xie et al., 2020; Jia et al., 2018; Ayop et al., 2018). The modeling of IFOBC is described in the subsequent subsections.

2.2.1. Interleaved fractional order boost converter

Two fractional-order boost converters, operating with a phase shift of 180 degrees between them, are interleaved to create an Interleaved Fractional-Order Boost Converter (IFOBC). To minimize conduction losses and input leakage current, the IFOBCs are operated in Continuous Conduction Mode (CCM). The IFOBC consists of four switches (two controlled ($IGBT_1$ & $IGBT_2$) and two uncontrolled (d_1 & d_2), one variable capacitor (C_{out}^β), and two variable inductors (L_1^α & L_2^α). The current through L_1^α & L_2^α is represented by i_{L_1} and i_{L_2} . The current

through C_{out}^β is $I_{C_{out}^\beta}(t)$. The controlled switching device is IGBT, while the uncontrolled switching device is diode. The voltages ($V_{L_1^\alpha}(t)$ and $V_{L_2^\alpha}(t)$) across the fractional-order inductors (L_1^α & L_2^α) are represented as in Equation (1).

$$V_{L_1^\alpha}(t) = L_1^\alpha \frac{d^\alpha i_{L_1}}{dt^\alpha}; \quad V_{L_2^\alpha}(t) = L_2^\alpha \frac{d^\alpha i_{L_2}}{dt^\alpha}; \quad (1)$$

The current through the fractional capacitor (C_{out}^β) is represented in Equation (2).

$$I_{C_{out}^\beta}(t) = C_{out}^\beta \frac{d^\beta V_C}{dt^\beta} \quad (2)$$

The average values of input voltage (V_{in}), output voltage (V_b), inductor current (i_{L_1} & i_{L_2}), current through Insulated Gate Bipolar Transistor (IGBT) (i_{S_2} & i_{S_1}), and duty cycle (D) are $\overline{V_{in}}, \overline{V_b}, \overline{i_{L_1}}, \overline{i_{L_2}}, \overline{i_{S_1}}, \overline{i_{S_2}}$, and \overline{D} . The small signal equivalences are represented by $\tilde{V}_{in}, \tilde{V}_b, \tilde{i}_{L_1}, \tilde{i}_{L_2}, \tilde{i}_{S_1}, \tilde{i}_{S_2}$, and \tilde{D} . The relationship between the variable, its small signal equivalences, and average equivalences is represented by Equation (3).

$$\overline{V_{in}} = V_{in} + \tilde{V}_{in}; \quad \overline{V_b} = V_b + \tilde{V}_b; \quad \overline{i_{L_1}} = i_{L_1} + \tilde{i}_{L_1}; \quad \overline{D} = D + \tilde{D}; \quad (3)$$

$$\overline{i_{S_1}} = i_{S_1} + \tilde{i}_{S_1}; \quad \overline{i_{L_2}} = i_{L_2} + \tilde{i}_{L_2}; \quad \overline{i_{S_2}} = i_{S_2} + \tilde{i}_{S_2};$$

The modified expression for the voltage across L_1^α and L_2^α , when the controlled switch is forward biased and the uncontrolled switch is reverse biased, is given by Equation (4).

$$V_{L_1^\alpha}(t) = \frac{\overline{V_{in}}}{L_1^\alpha} = \frac{d^\alpha i_{L_1}}{dt^\alpha}; \quad V_{L_2^\alpha}(t) = \frac{\overline{V_{in}}}{L_2^\alpha} = \frac{d^\alpha i_{L_2}}{dt^\alpha}; \quad (4)$$

The current through L_1^α & L_2^α is represented by Equation (5).

The current value represented by Equation (5) is the peak value of the current. The average value of the current through L^α is represented by Equation (6)

$$i_{L_1} = \frac{\overline{V_{in}}(D_1 T)^\alpha}{\alpha L_1^\alpha \Gamma(\alpha)}; \quad i_{L_2} = \frac{\overline{V_{in}}(D_1 T)^\alpha}{\alpha L_2^\alpha \Gamma(\alpha)} \quad (5)$$

$$\overline{i_{L_1}} = \frac{D_1 + D_2}{2} \cdot \frac{\overline{V_{in}}(D_1 T)^\alpha}{\alpha L_1^\alpha \Gamma(\alpha)}; \quad \overline{i_{L_2}} = \frac{D_1 + D_2}{2} \cdot \frac{\overline{V_{in}}(D_1 T)^\alpha}{\alpha L_2^\alpha \Gamma(\alpha)}; \quad (6)$$

T represents the total duration of on-time; D_1 represents the duty cycle when the IGBT is on and the diode is off. $T(\alpha)$ is the gamma function and it represents the continuous change in the fractional inductance. The current through the IGBTs (i_{S_1} & i_{S_2}) is mathematically expressed by Equation (7).

$$i_{S_1} = \frac{D_1 \overline{V_{in}}(D_1 T)^\alpha}{2\alpha L_1^\alpha \Gamma(\alpha)}; \quad i_{S_2} = \frac{D_1 \overline{V_{in}}(D_1 T)^\alpha}{2\alpha L_2^\alpha \Gamma(\alpha)}; \quad (7)$$

The average values of the inductor and diode voltages are represented by Equation (8).

$$\overline{v_{L_1}} = D_1 \overline{V_{in}} + D_2 (\overline{V_{in}} - \overline{V_b}); \quad \overline{v_{L_2}} = D_1 \overline{V_{in}} + D_2 (\overline{V_{in}} - \overline{V_b});$$

$$\overline{v_{d_1}} = -D_1 \overline{V_{in}} + (1 - D_1 - D_2) (\overline{V_{in}} - \overline{V_b});$$

$$\overline{v_{d_2}} = -D_1 \overline{V_{in}} + (1 - D_1 - D_2) (\overline{V_{in}} - \overline{V_b}) \quad (8)$$

The average voltage across L_1^α & L_2^α is always zero, because the inductor L_1^α & L_2^α is considered ideal. Therefore, the value of D_2 (which is the duty cycle when $IGBT_2$ is off and the diode, d_2 , is conducting) is represented by Equation (9).

$$D_2 = \frac{D_1 \overline{V_{in}}}{-(\overline{V_{in}} - \overline{V_b})} \quad (9)$$

Substituting the value of D_2 in Equation (6), it is re-modified into Equation (10).

$$\overline{i_{L_1}} = \frac{D_1 \overline{V_b}}{-2(\overline{V_{in}} - \overline{V_b})} \cdot \frac{\overline{V_{in}}(D_1 T)^\alpha}{\alpha L_1^\alpha \Gamma(\alpha)}; \quad \overline{i_{L_2}} = \frac{D_1 \overline{V_b}}{-2(\overline{V_{in}} - \overline{V_b})} \cdot \frac{\overline{V_{in}}(D_1 T)^\alpha}{\alpha L_2^\alpha \Gamma(\alpha)}; \quad (10)$$

After linearizing the fractional inductors and fractional capacitor, it is imperative to remove the small signal values. The currents through IGBTs (i_{S_1} & i_{S_2}) and L_1^α & L_2^α after omitting the small signal terms are stated by Equation (11).

$$\begin{aligned} i_{S_1} &= \frac{V_{in} T^\alpha D_1^{1+\alpha}}{2\alpha L_1^\alpha T(\alpha)}; & i_{L_1} &= \frac{D_1 V_{in}}{-2(V_{in}-V_b)} \cdot \frac{V_b(D_1 T)^\alpha}{\alpha L_1^\alpha T(\alpha)}; \\ i_{S_2} &= \frac{V_{in} T^\alpha D_1^{1+\alpha}}{2\alpha L_2^\alpha T(\alpha)}; & i_{L_2} &= \frac{D_1 V_{in}}{-2(V_{in}-V_b)} \cdot \frac{V_b(D_1 T)^\alpha}{\alpha L_2^\alpha T(\alpha)}; \end{aligned} \quad (11)$$

The operation of IFOBC is explained in four operating modes. The operating modes are as follows:

- Mode-1: switches ($IGBT_1$ & $IGBT_2$) are on and diodes (d_1 & d_2) are off.
- Mode-2: $IGBT_1, d_2$ are on and $d_1, IGBT_2$ are off.
- Mode-3: $d_1, IGBT_2$ are on and $IGBT_1, d_2$ are off.
- Mode-4: switches ($IGBT_1$ & $IGBT_2$) are off and diodes (d_1 & d_2) are on.

In Mode-1, the switches ($IGBT_1$ & $IGBT_2$) are turned on, while the diodes (d_1 & d_2) are in the off state. The voltage across the capacitor, C_{out}^β , and the two line currents (current through L_1^α & L_2^α) are represented by Equation (12).

$$\begin{aligned} \frac{di_{L_1}}{dt} &= \frac{d}{dt} \frac{D_1 V_{in}}{-2(V_{in}-V_b)} \cdot \frac{V_b(D_1 T)^\alpha}{\alpha L_1^\alpha T(\alpha)}; & \frac{di_{L_2}}{dt} &= \frac{d}{dt} \frac{D_1 V_{in}}{-2(V_{in}-V_b)} \cdot \frac{V_b(D_1 T)^\alpha}{\alpha L_2^\alpha T(\alpha)}; \\ \frac{dv_b}{dt} &= \frac{1}{C_{out}^\beta} \frac{d}{dt} \frac{D_1 V_{in}}{-2(V_{in}-V_b)} \cdot \frac{V_b(D_1 T)^\alpha}{\alpha L_2^\alpha T(\alpha)}; \end{aligned} \quad (12)$$

In Mode-2, $IGBT_1, d_2$ are conducting and $d_1, IGBT_2$ are reverse biased. The equations are represented by Equation (13).

$$\begin{aligned} \frac{di_{L_1}}{dt} &= \frac{d}{dt} \frac{D_1 V_{in}}{-2(V_{in}-V_b)} \cdot \frac{V_b(D_1 T)^\alpha}{\alpha L_1^\alpha T(\alpha)}; & \frac{di_{L_2}}{dt} &= \frac{d}{dt} \frac{D_1 V_{in}}{-2(V_{in}-V_b)} \cdot \frac{V_b(D_1 T)^\alpha}{\alpha L_2^\alpha T(\alpha)} - \frac{V_b}{L_2^\alpha}; \\ \frac{dv_b}{dt} &= \frac{1}{C_{out}^\beta} \frac{d}{dt} \frac{D_1 V_{in}}{-2(V_{in}-V_b)} \cdot \frac{V_b(D_1 T)^\alpha}{\alpha L_2^\alpha T(\alpha)} - \frac{V_b}{RC_{out}^\beta}; \end{aligned} \quad (13)$$

In Mode 3, $IGBT_1, d_2$ are reverse biased and $d_1, IGBT_2$ are forward biased. The equations are represented by Equation (14).

$$\begin{aligned} \frac{di_{L_1}}{dt} &= \frac{d}{dt} \frac{D_1 V_{in}}{-2(V_{in}-V_b)} \cdot \frac{V_b(D_1 T)^\alpha}{\alpha L_1^\alpha T(\alpha)} - \frac{V_b}{L_1^\alpha}; & \frac{di_{L_2}}{dt} &= \frac{d}{dt} \frac{D_1 V_{in}}{-2(V_{in}-V_b)} \cdot \frac{V_b(D_1 T)^\alpha}{\alpha L_2^\alpha T(\alpha)}; \\ \frac{dv_b}{dt} &= \frac{1}{C_{out}^\beta} \frac{d}{dt} \frac{D_1 V_{in}}{-2(V_{in}-V_b)} \cdot \frac{V_b(D_1 T)^\alpha}{\alpha L_2^\alpha T(\alpha)} - \frac{V_b}{RC_{out}^\beta}; \end{aligned} \quad (14)$$

In Mode-4, the switches ($IGBT_1$ & $IGBT_2$) are turned non-conducting, while the diodes (d_1 & d_2) are in the conducting state. The equations are represented by Equation (15).

$$\begin{aligned} \frac{di_{L_1}}{dt} &= \frac{d}{dt} \frac{D_1 V_{in}}{-2(V_{in}-V_b)} \cdot \frac{V_b(D_1 T)^\alpha}{\alpha L_1^\alpha T(\alpha)} - \frac{V_b}{L_1^\alpha}; \\ \frac{di_{L_2}}{dt} &= \frac{d}{dt} \frac{D_1 V_{in}}{-2(V_{in}-V_b)} \cdot \frac{V_b(D_1 T)^\alpha}{\alpha L_2^\alpha T(\alpha)} - \frac{V_b}{L_2^\alpha}; \\ \frac{dv_b}{dt} &= \frac{1}{C_{out}^\beta} \frac{d}{dt} \frac{D_1 V_{in}}{-2(V_{in}-V_b)} \cdot \frac{V_b(D_1 T)^\alpha}{\alpha L_1^\alpha T(\alpha)} + \frac{1}{C_{out}^\beta} \frac{d}{dt} \frac{D_1 V_{in}}{-2(V_{in}-V_b)} \cdot \frac{V_b(D_1 T)^\alpha}{\alpha L_2^\alpha T(\alpha)} - \frac{V_b}{RC_{out}^\beta}; \end{aligned} \quad (15)$$

2.3. 15-Level Reduced switch multilevel inverter

The choice of inverter for the proposed work is a symmetrical 15-level Reduced Switch Multilevel Inverter (RSMI). Figure 1(c) contains the model RSMI. The RSMI is an improvement on the cascaded h bridge concepts (Izci et al., 2022; Eker et al., 2021). Reducing the number of controlled switches while maintaining the same number of source requirements contributes to the improvement of the proposed system's performance. The main reason for using RSMI is its ability to reduce voltage stress on components, eliminate the need for transformers, improve Electro Magnetic Compatibility (EMC), and reduce Total Harmonic Distortion (THD) in the proposed system.

$$\text{Number of controlled switches} = \frac{Lev+5}{2} \quad (16)$$

$$\text{Number of sources} = \frac{Lev-1}{2} \quad (17)$$

where Lev is the level of the inverter. Equation (16) and Equation (17) define the requirements including the number of switches and the number of sources for RSMI. It is evident from Equation (16) and Equation (17) that the number of switches and sources for a 15-level RSMI is 10 and 7, respectively. The 15-level RSMI is chosen because, below the 15 levels, enough harmonic distortions exist, while above the 15 levels, the switching technique becomes vexed with reduced or hardly improved performance. The IGBTs are named chronologically $IGBT_{10}$. The sources are named **DC1 - DC10** orderly. All seven sources are connected to the IFOBC.

2.3.1. Harmonic

The measure of all components of the harmonic present in an electrical current signal is termed the total harmonic distortion. The extensive utilization of power electronics-based switches leads to the generation of harmonic distortions in electrical signals and it is represented symbolically by thd_i . Harmonics in electricity systems can lead to various adverse effects, including circuit breaker tripping, decreased power factor, increased heat generation, reduced efficiency, and elevated electromagnetic emissions. It is desirable to maintain thd_i at a low value as it reduces peak current and improves power factor and efficiency. thd_i is measured in compliance with IEEE-519 standard (Marrero et al., 2022).

2.4. Support Vector Pulse Width Modulation (SVPWM)

The SVPWM employs discrete switching for flux compensation (Logeswaran et al., 2015; Guohua et al., 2022; Nguyen et al., 2022; Lin et al., 2020). The space vector diagram is the hexagon consisting of 6 sectors. Each sector is represented by an equilateral triangle with sides of equal length. The height of the equilateral triangle is $\frac{\sqrt{3}}{2}$. The three-phase references used for the design of SVPWM are described by Equation (18).

$$\left. \begin{aligned} V_a &= V_{ma} \sin \omega t; & V_b &= V_{mb} \sin \left(\omega t - \frac{2\pi}{3} \right); \\ V_c &= V_{mc} \sin \left(\omega t + \frac{2\pi}{3} \right); \end{aligned} \right\} \quad (18)$$

In this modulation technique, the three-phase modulation signals are converted into two-phase quantities. This conversion is achieved by Clarke's transformation. The transformation into two-phase quantities by Clarke transformation is represented by Equation (19).

$$\begin{bmatrix} V_\alpha \\ V_\beta \end{bmatrix} = \frac{2}{3} \begin{bmatrix} 1 & -\frac{1}{2} & -\frac{1}{2} \\ 0 & \frac{\sqrt{3}}{2} & -\frac{\sqrt{3}}{2} \end{bmatrix} \begin{bmatrix} V_a \\ V_b \\ V_c \end{bmatrix} \quad (19)$$

The angle between the two-phase components is represented by θ . θ is defined mathematically in Equation (20).

$$\theta = \tan^{-1} \left(\frac{V_\beta}{V_\alpha} \right) \quad (20)$$

The reference vector is generated by Equation (21):

$$V_1 = V^* \sin \gamma; \quad V_2 = V^* \cos \gamma; \quad (21)$$

where γ is the angle in the sector and defined mathematically by Equation (22); the range of γ is $0 \leq \gamma \leq 60^\circ$ and V^* represents the maximum magnitude that is mathematically represented by Equation (23).

$$\gamma = \text{rem} \left(\frac{\theta}{360} \right) \quad (22)$$

$$V^* = \sqrt{V_\alpha^2 + V_\beta^2} \quad (23)$$

The operating sector number (S) is calculated using Equation (24). The maximum number of the sectors is 6.

$$S = \text{floor} \left(\left(\frac{3\theta}{\pi} \right) + 1 \right) \quad (24)$$

The range of θ is $0 \leq \theta \leq 360^\circ$. In each sector, there are two types of triangles. The first type has a base at the bottom and the second has a base side at the top. The number of the triangles can be efficiently determined using two integer variables (P_1 & P_2). The values (P_1 & P_2) are dependent upon (V_1 & V_2), respectively, as represented in Equation (25):

$$P_1 = \text{int} \left(V_1 + \frac{V_2}{\sqrt{3}} \right); \quad P_2 = \text{int} \left(\frac{V_2}{n} \right); \quad (25)$$

Let ($V_{\alpha i}, V_{\beta i}$) be the coordinates of the reference vector concerning the origin of the rhombus. The slope of the line represented by the coordinates ($V_{\alpha i}, V_{\beta i}$) is compared with the slope of the rhombus ($\sqrt{3}$). Two possible cases are $V_{\beta i} \leq \sqrt{3}V_{\alpha i}$ and $V_{\beta i} \geq \sqrt{3}V_{\alpha i}$, as shown in Table 2.

Table 2. Slope comparison with rhombus.

$V_{\beta i} \leq \sqrt{3}V_{\alpha i}$	$V_{\beta i} \geq \sqrt{3}V_{\alpha i}$
$\left. \begin{array}{l} V_{\beta i} \leq \sqrt{3}V_{\alpha i} \\ \Delta_n = P_1^2 + 2P_2 \\ V_3 = V_{\alpha i} \\ V_4 = V_{\beta i} \end{array} \right\}$	$\left. \begin{array}{l} V_{\beta i} \geq \sqrt{3}V_{\alpha i} \\ \Delta_n = P_1^2 + 2P_2 + 1 \\ V_3 = 0.5 - V_{\alpha i} \\ V_4 = n - V_{\beta i} \end{array} \right\}$

where Δ_n is an integer that signifies the n^{th} triangle in space. The equation provides a simple way for ordering all triangles to facilitate faster identification and applicability to other levels. The on-time is calculated using Equations (26-28)

$$T_\alpha = T_S \left[V_3 - \frac{V_4 T_S}{2n} \right] \quad (26)$$

$$T_\beta = T_S \left[\frac{V_4}{n} \right] \quad (27)$$

$$T_0 = T_S - T_\alpha - T_\beta \quad (28)$$

where, T_α is on time for V_α , T_β is on time for V_β , T_0 is on time of zero vector, and T_S is switching time.

2.5. Electromagnetic interference filter

Electro Magnetic Interference (EMI) is an unnecessary signal that affects the electrical circuitry. It is radiated from any power electronics-based components present in the circuit (Yao et al., 2021). The EMI is categorized as Conducted EMI (CEMI) and Radiated EMI (REMI). Lower frequency disturbances are caused by CEMI, while higher frequency disturbances are caused by REMI. The CEMI has a frequency range of 10 KHz to 30 KHz. REMI emissions are in the frequency range between 30MHz and 1GHz. Converters are the main source of EMI due to pulsating input currents and rapidly changing voltages. The EMI filters, when designed with the aid of passive components, are called Passive EMI filters (PEFs). PEFs are used to suppress the CEMI. Table 3 presents the frequency limits for conducted emissions. Conducted emissions are regulated by Comité International Spécial des Perturbations Radioélectriques (CISPR) 22 over the frequency range of 150 KHz to 30 MHz.

Table 3. CISPR 22 for conducted Emission limits.

Frequency (MHz)	Conducted Limit (dB μ V)	
	Quasi Peak	Average
0.15-0.5	79	66
0.5-30	73	60

The EMI measurement procedure requires a 50W/50mH Line Impedance Stabilization Network (LISN) to be inserted

between the equipment under the test (EUT). Here EUT is a DC-DC converter. LISN is used to separate radio frequency disturbances from power signals. LISN is placed between the DC source and the IFOBC.

2.5.1. Passive EMI filter

The PEF is a CLC-type π filter used for CM & DM noise rejection. The basic structure of PEF is represented in Figure 2(a). The objective of using PEF is to maximize the impedance gap between the filter and connected systems. The main components of PEF are common mode inductance (L_{cm}), differential mode inductance (L_{dm}), common mode capacitor (C_{cm}), and differential mode capacitance (C_{dm}). To facilitate the analysis of maximum impedance mismatch in the transmission line (T), a parameter matrix analysis is conducted in the circuit. The mathematical representation of the T parameter matrix is represented by Equation (29).

$$\begin{bmatrix} V_{sp} \\ I_s \end{bmatrix} = \begin{bmatrix} T_{11} & T_{12} \\ T_{21} & T_{22} \end{bmatrix} * \begin{bmatrix} V_{in} \\ -I_{sp} \end{bmatrix} \quad (29)$$

The T parameters (T_{11}, T_{12} , T_{21} , and T_{22}) are defined mathematically by Equation (30).

$$T_{11} = 1 - \omega^2 L_{cm} C_y \Big|_{V_{in}, I_{sp}=0}; \quad T_{12} = j\omega L_{cm} = \frac{V_{sp}}{I_s} \Big|_{V_{in}=0}; \quad (30)$$

$$T_{21} = j\omega C_1 = \frac{I_s}{V_{in}} \Big|_{I_{sp}=0}; \quad T_{22} = 1 = \frac{I_s}{I_{sp}} \Big|_{V_{in}=0};$$

The voltage from the solar panel (V_{sp}) V_j is expressed in terms of V_{dt} as in Equation (31).

$$V_{in} = \frac{V_{dt}}{T_{11} + \frac{T_{12} + T_{21}R_s + T_{22}R_s}{R_s}}; \quad V_{sp} = \frac{V_{dt}R_s}{R_s + R_t}; \quad (31)$$

The filter insertion loss (IL_{cm}) is a measure of the efficacy of PEFs. The mathematical equivalence of filter insertion loss is represented by Equation (32).

$$IL_{cm} = 20 \log \frac{V_{sp}}{V_{in}} = 20 \log \left| \frac{j\omega L_{cm} + (1 - \omega^2 L_{cm} C_y)R_s + R_t + j\omega R_s R_t C_y}{R_s + R_t} \right| \quad (32)$$

The mathematical expression for L_{cm} and L_{dm} is represented in Equation (33).

$$L_{cm} = \frac{1}{2C_y} \left(\frac{1}{2 \times \pi \times f_m} \right)^2; \quad L_{dm} = \frac{1}{2C_x} \left(\frac{1}{2 \times \pi \times f_m} \right)^2 \quad (33)$$

The leakage current (I_q) resulting from the effects of ground capacitance (C_y) is represented by Equation (34). f_m represents the input frequency which is 50hz in the proposed model and V_m is the non-zero ground voltage drop.

$$I_q = 2 \times \pi \times f_m \times C_y \times V_m \quad (34)$$

The magnitude of I_q under normal operating conditions is less than 0.5 mili ampere. Table 2 represents the values of the EMI filter components. The EMI disturbance plot for IFOBC without PEF is represented in Figure 2 (b). It is evident from the figure that there are some disturbances resulting from the nonlinearities. The use of PEF is highlighted in Figure 2 (c). The use of PEF reduced the nonlinearities, thus improving the response of the proposed system and necessitating the use of PEF.

Table 4. The values of the EMI filter components.

Filter Parameter	Values
$C_{y_{max}}$	7.238nf
C_{y_1}, C_{y_2}	6.8nf
C_{x_1}, C_{x_2}	330nf
L_{cm}	4.2 mH
L_{dm}	6.7 μ H

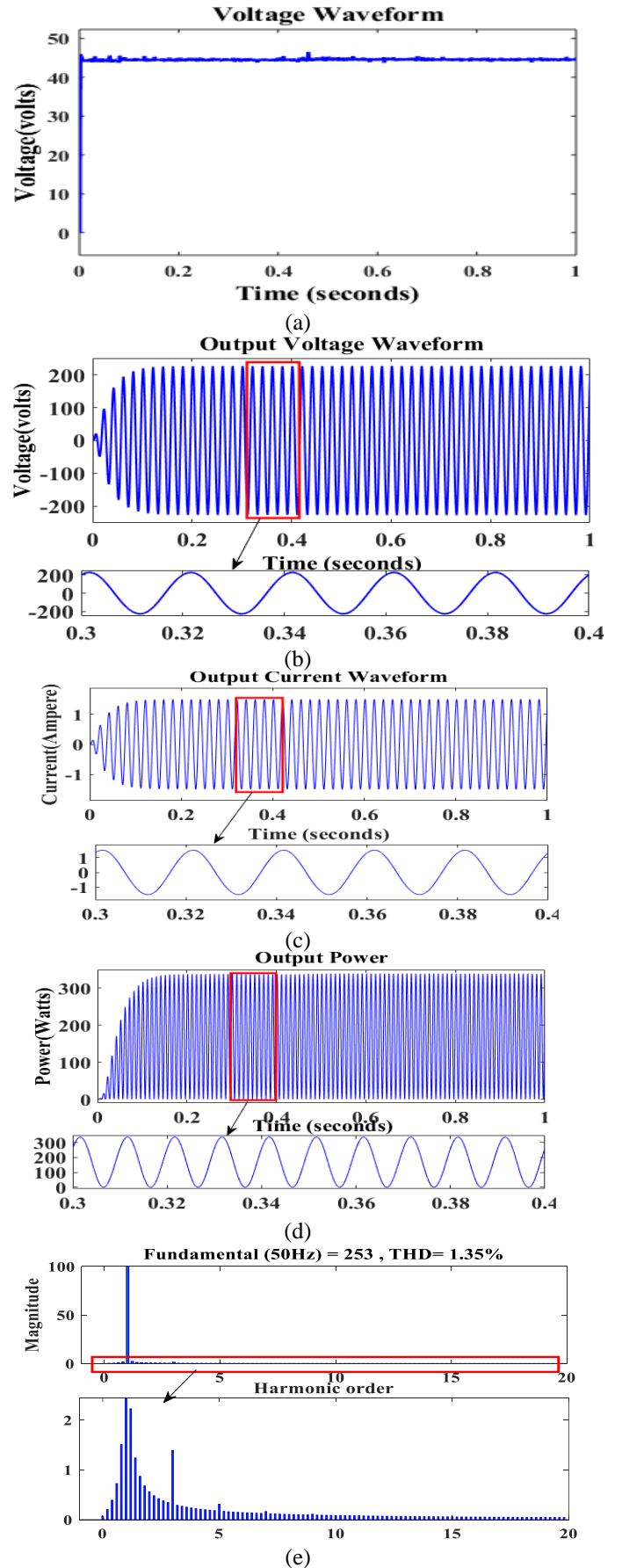
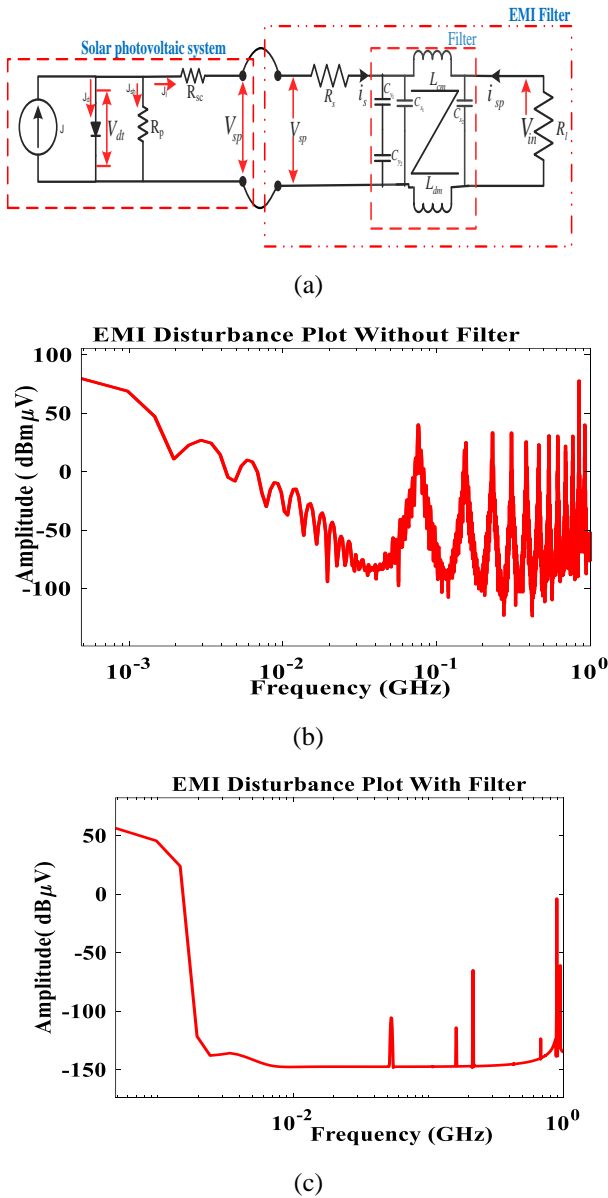


Figure 2. (a) Basic structure for PEFs; (b) EMI disturbance plot for IFOBC without PEF; (c) EMI disturbance plot for IFOBC with PEF.

2.6. Open loop response

The photovoltaic system under open-loop conditions is discussed in the affixing sub-sections.

2.6.1. Open loop IFOBC

In an open loop, the IGBT used in IFOBC is triggered using a pulse generator operating at 30 Kilo Hertz (KHz). The input to the IFOBC is 24 volts, while the output increases to 47 volts. V_b is depicted in Figure 3(a). The presence of the ripple voltage of magnitude 1.02 volts results from the absence of proper control mechanisms. The main source of ripple in the response of IFOBC is the presence of nonlinearities.

Figure 3. Open loop parameters of a photovoltaic system: (a) V_b plot; (b) V_{inv} plot; (c) I_{inv} plot; (d) P_{inv} plot; (e) thd_i plot.

2.6.2. Open-loop RSMI

The IGBTs present in the RSMI are triggered using the SVPWM technique at 30 KHz. The magnitude of V_{inv} and current from 15-level RSMI (I_{inv}) are 226 volts and 2 Amperes, as represented in Figure 3(b-c). The power (P_{inv}) delivered to the load is 390 watts, as depicted in Figure 3(d). The total harmonic distortion (thd_i) for the output current of 15-level RSMI is 1.35 %, as represented in Figure 3(e). The results obtained from the open-loop circuit indicate the potential for further improvement by implementing appropriate control techniques.

3. CONTROL ALGORITHMS

In this section, Hybrid Teaching Learning Based-Horse Herd Optimization Algorithm regulated Fractional Order Tilt Acceleration Derivative with Filter (HTLB-HHOA regulated FOTADF) is discussed in detail. The performance of TLBO-HHOA-regulated FOTDAF controller-based photovoltaic systems is studied in terms of stability, accuracy, and robustness. The controller performance indices such as $thd_i, V_{inv}, I_{inv}, P_{inv}$, and V_b are analyzed with appropriate justification for the controller performance (Tufenkci et al., 2020; Yao et al., 2021; Eberlein, et al., 2021). TLBO-HHOA regulated FOTDAF stands defined in the appending sub-sections.

3.1. TLBO-HHOA regulated FOTDAF

The TLBO-HHOA-regulated FOTDAF used in the proposed photovoltaic system is depicted in Figure 4(a). The controller output is the control signal ($u(t)$), while the input signal is the error signal ($e(t)$). The transfer function (TF) for the TLBO-HHOA regulated FOTDAF was already expressed in (Patra et al., 2020; Patra et al., 2021), as also represented in Equation (35)

$$TF = (K_t \times s^n) + K_d \left(\frac{N_3 \times s^\gamma}{N_3 + s^\gamma} \right) + K_a \left(\frac{N_2 \times N_1 \times s^{\alpha+\beta}}{(s^\alpha + N_1)(s^\beta + N_2)} \right) \quad (35)$$

where tilt gain is K_t , acceleration gain is K_a , the derivative gain is K_d , the coefficient of tilt is n , pre-filter gains are N_1, N_2, N_3 , coefficients of accelerations are α, β , and coefficient of the derivative is γ . The control parameters are evaluated based on the response of the photovoltaic system to the fitness function. The proposed model utilizes Integral Time Absolute Error (ITAE) as its fitness function. Equation (36) represents the mathematical principle for ITAE.

$$ITAE = \int_0^\infty |e(t)| \times t \times dt \quad (36)$$

where $|e(t)|$ denotes the magnitude of the error signal. The enhanced response of the proposed photovoltaic system is achieved through a lower value of ITAE. The optimal values of control parameters are pre-determined by the HTLB-HHOA method for better control V_{inv} (Eker et al., 2021). The structure of the proposed control technique is presented in Figure 4(a).

3.2. Parameter optimization

The tuning of the proposed FOTDAF controller is achieved by two optimization techniques, i.e., HHOA and TLBO.

3.2.1. HHOA

HHOA is based on the behavior of horses in their natural living habitat. The behavior of horses includes grazing (\bar{G}), hierarchy (\bar{H}), sociability (\bar{S}), imitation (\bar{I}), defense mechanism (\bar{D}), and roam (\bar{R}). The movement of horses is mathematically modeled for the current iteration ($iter$) and is represented by Equation (37).

$$X_m^{iter.age} = \bar{V}_m^{iter.age} + X_m^{(iter-1).age} \quad (37)$$

where X_m is the position of the m^{th} horse, age is the age range of horses, and V_m is the velocity vector of the horses. The age range for horses is α, β, γ , and δ . The age of α horses is above 15 years. The age of β horses ranges between 10 and 15 years. The age of γ horses is between 5 and 10 years. The age of δ horses is below 5 years. The age of horses is selected by the comprehensive matrix of responses. This matrix is sorted based on the best responses and consequently, the first 10% of the horses from the top are selected as α horses. The next 20% are grouped as β horses. γ and δ account for 30% and 40% of the remaining horses. The six behaviors of horses are mathematically implemented to detect the velocity vector. The motion vector of horses at different ages during each cycle of the algorithm is expressed by Equations (38-41).

$$\bar{V}_m^{iter.\alpha} = \bar{G}_m^{iter.\alpha} + \bar{D}_m^{iter.\alpha} \quad (38)$$

$$\bar{V}_m^{iter.\beta} = \bar{G}_m^{iter.\beta} + \bar{D}_m^{iter.\beta} + \bar{H}_m^{iter.\beta} + \bar{S}_m^{iter.\beta} \quad (39)$$

$$\bar{V}_m^{iter.\gamma} = \bar{G}_m^{iter.\gamma} + \bar{D}_m^{iter.\gamma} + \bar{H}_m^{iter.\gamma} + \bar{S}_m^{iter.\gamma} + \bar{I}_m^{iter.\gamma} + \bar{R}_m^{iter.\gamma} \quad (40)$$

$$\bar{V}_m^{iter.\delta} = \bar{G}_m^{iter.\delta} + \bar{I}_m^{iter.\delta} + \bar{R}_m^{iter.\delta} \quad (41)$$

where $\bar{G}_m^{iter.\alpha}$ represents the grazing vector for the age group α during the current iteration, $\bar{D}_m^{iter.\alpha}$ the defense mechanism vector for the age group α during the current iteration, $\bar{G}_m^{iter.\beta}$ the grazing vector for the age group β during the current iteration, $\bar{D}_m^{iter.\beta}$ the defense mechanism vector for the age group β during the current iteration, $\bar{H}_m^{iter.\beta}$ the hierarchy vector for the age group β during the current iteration, $\bar{S}_m^{iter.\beta}$ the sociability vector for the age group β during the current iteration, $\bar{G}_m^{iter.\gamma}$ the grazing vector for the age group γ during the current iteration, $\bar{D}_m^{iter.\gamma}$ the defense mechanism vector for the age group γ during the current iteration, $\bar{H}_m^{iter.\gamma}$ the hierarchy vector for the age group γ during the current iteration, $\bar{S}_m^{iter.\gamma}$ the sociability vector for the age group γ during the current iteration, $\bar{I}_m^{iter.\gamma}$ the imitation vector for the age group γ during the current iteration and $\bar{R}_m^{iter.\gamma}$ the roam vector for the age group γ during the current iteration, $\bar{G}_m^{iter.\delta}$ the grazing vector for the age group δ during the current iteration, $\bar{I}_m^{iter.\delta}$ the imitation vector for the age group δ during the current iteration, and $\bar{R}_m^{iter.\delta}$ the roam vector for the age group δ during the current iteration.

3.2.1.1 Grazing (\bar{G})

The horse mostly feeds upon grasses, plants, and fodders. The horses graze upon a certain area. HHOA models graze areas around each horse with a coefficient g . The mathematical implementation of grazing is represented by Equation (42).

$$\bar{G}_m^{iter.age} = \bar{g}_m^{iter.age} (\tilde{u} + \rho) X_m^{(iter-1)} \quad (42)$$

where $\bar{g}_m^{iter.age}$ represents the motion parameter of the m^{th} horse, \bar{u} represents the lower bound of grazing space, l the upper bound of grazing space, and ρ the random constant between 0 and 1. $\bar{g}_m^{iter.age}$ is the orientation of horses in the grazing area. It is defined mathematically by Equation (43).

$$\bar{g}_m^{iter.age} = \bar{g}_m^{(iter-1).age} \times \omega_g \quad (43)$$

where ω_g is the reduction factor per cycle for grazing behavior modeling.

3.2.1.2 Hierarchy (\bar{H})

The hierarchy is followed by the horses. Horses follow their leaders and adult stallions are selected based on this hierarchy law. The tendency of the horse to follow the most experienced and strongest horse is denoted by the coefficient h . It is defined mathematically by Equation (44).

$$\bar{H}_m^{iter.age} = h_m^{iter.age} (X_*^{(iter-1)} - X_m^{(iter-1)}) \quad (44)$$

where $\bar{H}_m^{iter.age}$ indicates the best horse position on the velocity parameter; $X_*^{(iter-1)}$ indicates the location of the best horse; and $h_m^{iter.age}$ indicates the orientation of horses in the age group (α , β , and γ) towards hierarchy. It is defined mathematically by Equation (45).

$$\bar{h}_m^{iter.age} = \bar{h}_m^{(iter-1).age} \times \omega_h \quad (45)$$

where ω_h is the reduction factor per cycle for hierarchy behavior modeling.

3.2.1.3 Sociability (\bar{S})

The sociability behavior of horses is considered as a movement towards the average position of other horses. It is represented mathematically by the factors. The horses aged between 5-15 years (β and γ) are interested in socializing. It is expressed mathematically by Equation (46).

$$\bar{s}_m^{iter.age} = \bar{s}_m^{iter.age} \left(\left[\frac{1}{N} \sum_{j=1}^N X_j^{(iter-1)} \right] - X_m^{(iter-1)} \right) \quad (46)$$

where $\bar{s}_m^{iter.age}$ indicates the social motion vector of the i^{th} horse, N indicates the total number of horses, and $\bar{s}_m^{iter.age}$ the orientation of concerned horses towards the herd. It is defined mathematically by Equation (47).

$$\bar{s}_m^{iter.age} = \bar{s}_m^{(iter-1).age} \times \omega_s \quad (47)$$

where ω_s is the reduction factor per cycle for socializing behavior modeling.

3.2.1.4 Imitation (\bar{I})

In the optimization algorithm, the imitation behavior of horses is considered by the factor i . The mimic behavior of horses is expressed mathematically by Equation (48).

$$\bar{i}_m^{iter.age} = \bar{i}_m^{iter.age} \left(\left[\frac{1}{pN} \sum_{j=1}^N \bar{X}_j^{(iter-1)} \right] - X^{(iter-1)} \right) \quad (48)$$

where $\bar{i}_m^{iter.age}$ indicates the motion vector of the i^{th} horse towards the average of best horses with \bar{X} locations, pN is the total number of horses with the best locations, and $\bar{i}_m^{iter.age}$ is the orientation of concerned horses towards the motion of horses towards the average of the best horses. It is defined mathematically by Equation (49).

$$\bar{i}_m^{iter.age} = \bar{i}_m^{(iter-1).age} \times \omega_i \quad (49)$$

where ω_i is the reduction factor per cycle for the motion of horses towards the average of the best horses.

3.2.1.5 Defense Mechanism (\bar{D})

Flight or fight mechanisms are used by horses to defend themselves. Horses' running away from other horses is an inappropriate response which is far away from optimal. The defense mechanism is characterized by a factor d . The defense mechanism of horses is presented with a negative coefficient to keep the horses away from appropriate positions. The defense mechanism is modeled mathematically and represented by Equation (50).

$$\bar{D}_m^{iter.age} = -\bar{d}_m^{iter.age} \left(\left[\frac{1}{qN} \sum_{j=1}^{qN} \bar{X}_j^{(iter-1)} \right] - X^{(iter-1)} \right) \quad (50)$$

where $\bar{D}_m^{iter.age}$ indicates the escape vector of the i^{th} horse towards the average of the worst horses with \bar{X} locations, qN the total number of horses with the worst locations, and $\bar{d}_m^{iter.age}$ the orientation of concerned horses towards the motion of horses towards the average of the worst horses. It is defined mathematically by Equation (51).

$$\bar{d}_m^{iter.age} = \bar{d}_m^{(iter-1).age} \times \omega_d \quad (51)$$

where ω_d is the reduction factor per cycle for the escape of horses towards the average of the worst horses.

3.2.1.6 Roam (\bar{R})

The roaming behavior of horses is simulated by a random movement of factors r . Roaming is observed at younger ages and gradually disappears as the horse ages. This process is represented mathematically by Equation (52).

$$\bar{R}_m^{iter.age} = \bar{r}_m^{iter.age} (\rho X^{(iter-1)}) \quad (52)$$

where $\bar{R}_m^{iter.age}$ indicates the random velocity vector of the i^{th} horse for a local search and an escape from local minima and $\bar{r}_m^{iter.age}$ is the orientation of concerned horses with random velocity vector for a local search and an escape from local minima. It is defined mathematically by Equation (53).

$$\bar{r}_m^{iter.age} = \bar{r}_m^{(iter-1).age} \times \omega_r \quad (53)$$

where ω_r is the reduction factor per cycle for the random velocity vector of horses towards the local search and an escape from local minima. The general velocity vector is obtained by substituting the values obtained from Equations (42-53) into Equations (38-41). The modified velocity vector is represented mathematically in Equations (54-57). The velocity vector for the age group α is represented by Equation (54).

$$\bar{V}_m^{iter.\alpha} = (\bar{g}_m^{(iter-1).\alpha} \times \omega_g)(\bar{u} + \rho l)X_m^{(iter-1)} + - (\bar{d}_m^{(iter-1).\alpha} \times \omega_d) \left(\left[\frac{1}{qN} \sum_{j=1}^{qN} \bar{X}_j^{(iter-1)} \right] - X^{(iter-1)} \right) \quad (54)$$

The velocity vector for the age group β is represented by Equation (55).

$$\bar{V}_m^{iter.\beta} = \left(\bar{g}_m^{(iter-1).\beta} \times \omega_g)(\bar{u} + \rho l)X_m^{(iter-1)} + - (\bar{d}_m^{(iter-1).\beta} \times \omega_d) \left(\left[\frac{1}{qN} \sum_{j=1}^{qN} \bar{X}_j^{(iter-1)} \right] - X^{(iter-1)} \right) + (\bar{h}_m^{(iter-1).\beta} \times \omega_h) (X_*^{(iter-1)} - X_m^{(iter-1)}) + (\bar{s}_m^{(iter-1).\beta} \times \omega_s) \left(\left[\frac{1}{N} \sum_{j=1}^N X_j^{(iter-1)} \right] - X_m^{(iter-1)} \right) \right) \quad (55)$$

The velocity vector for the age group γ is represented by Equation (56).

$$\bar{v}_m^{iter,\gamma} = \left. \begin{aligned} & (\bar{g}_m^{(iter-1),\gamma} \times \omega_g)(\bar{u} + \rho l)X_m^{(iter-1)} + (\bar{r}_m^{(iter-1),\gamma} \times \omega_r) \\ & \quad (\rho X^{(iter-1)}) + \\ & - (\bar{d}_m^{(iter-1),\gamma} \times \omega_d) \left(\left[\frac{1}{qN} \sum_{j=1}^q \bar{X}_j^{(iter-1)} \right] - X^{(iter-1)} \right) \\ & + (\bar{h}_m^{(iter-1),\gamma} \times \omega_h) (X_*^{(iter-1)} - X_m^{(iter-1)}) \\ & + (\bar{s}_m^{(iter-1),\gamma} \times \omega_s) \left(\left[\frac{1}{lN} \sum_{j=1}^l X_j^{(iter-1)} \right] - X_m^{(iter-1)} \right) \\ & + (\bar{r}_m^{(iter-1),\gamma} \times \omega_i) \left(\left[\frac{1}{pN} \sum_{j=1}^p \hat{X}^{(iter-1)} \right] - X^{(iter-1)} \right) \end{aligned} \right\} \quad (56)$$

The velocity vector for the age group δ is represented by Equation (57).

$$\bar{v}_m^{iter,\delta} = \left. \begin{aligned} & (\bar{g}_m^{(iter-1),\delta} \times \omega_g)(\bar{u} + \rho l)X_m^{(iter-1)} \\ & + (\bar{i}_m^{(iter-1),\delta} \times \omega_i) \left(\left[\frac{1}{pN} \sum_{j=1}^p \hat{X}^{(iter-1)} \right] - X^{(iter-1)} \right) \\ & + (\bar{r}_m^{(iter-1),\delta e} \times \omega_r) (\rho X^{(iter-1)}) \end{aligned} \right\} \quad (57)$$

The optimization is carried out until the maximum iteration limit is reached or the iteration limits are reached.

3.2.2. TLBO

TLBO is an algorithm that deals with the influence of a teacher on the outcome of learners. The teacher works hard and educates the learners. The educated learners discuss amongst themselves and improve upon and modify the knowledge gained. In this algorithm, there are two modes of learning: learning through the teacher and learning by interacting with other learners. It is assumed that two teachers teach the same subject with the same content to learners of a similar level in two different classes. The normal distribution obtained for the marks is defined mathematically by Equation (58).

$$f(Z) = \frac{1}{\sigma\sqrt{2\pi}} e^{-\frac{(x-\mu)^2}{2\sigma^2}} \quad (58)$$

where σ^2 is the variance, μ is the mean, and Z is any value (marks obtained) for which standard deviation is calculated. In TLBO, the teaching method is mimicked and used for optimization. When the teacher teaches the learners, then he transmits his knowledge to the learners. The learners after gaining knowledge from the teacher are considered equal to the teachers. The learners can improve upon their knowledge base by interacting amongst themselves. This feature of the teaching-learning process is mimicked for optimization purposes. Like other nature-inspired algorithms, TLBO is a population-based algorithm. The population in TLBO is a class of learners. In TLBO, the number of subjects is analogous to the number of design variables. The result scored by learners is analogous to the result of the evaluation of fitness function. The Teacher is considered the best fit in TLBO.

3.2.2.1. Teachers phase

Under idyllic conditions, a good teacher brings the knowledge of learners of a class to his level. However, this is not the case in practice the teachers can improve the mean knowledge of learners to a certain level only depending upon the capability of learners. At any iteration i , M_i is the mean and the teacher T_i will try M_i to its level. Therefore, now, the new mean is M_{new_i} . The solution is getting updates as per the difference

($MeanDiff_i$) between existing and new means. This is represented mathematically by Equation (59).

$$MeanDiff_i = r_i(M_{new_i} - \Pi M_i) \quad (59)$$

where r_i and Π represent the random number with a range [0,1] and teaching factor, respectively. Π can have values of 1 or 2, which is decided as per the mathematical equation (60).

$$\Pi = round(1 + rand(0,1)\{2 - 1\}) \quad (60)$$

$MeanDiff_i$ modifies the existing solutions as per the mathematical equation (61).

$$Z_{new,i} = Z_{old,i} + MeanDiff_i \quad (61)$$

3.2.2.2. Learners phase

Learners improve upon their knowledge by interacting amongst themselves and gaining from inputs given by teachers. Learners can learn from other learners having higher knowledge by interacting with them. The methods for interaction like group discussion, presentation, and direct and indirect communication. The choice of methods depends upon the learners. For two learners k and p , the updates on marks obtained are expressed mathematically by Equation (62).

$$\begin{aligned} \text{If: } f(Z_k) < f(Z_p) & \rightarrow Z_{new,k} = Z_{old,k} + r_1(Z_k - Z_p) \\ \text{Else: } f(Z_k) > f(Z_p) & \rightarrow Z_{new,k} = Z_{old,k} + r_1(Z_p - Z_k) \end{aligned} \quad (62)$$

If Z_{new} gives the best fitness value, then it is accepted as the best solution. The optimization is carried out till the limit of maximum iteration is reached or the iteration limits are reached.

3.2.3. HTLB-HHOA

The optimization (TLBO-HHOA) is a minimization type of optimization (Eker et al., 2021). This optimization technique hybridizes TLBO algorithm and HHOA. HHOA has global search capability with a slower convergence rate and TLBO has a faster convergence rate with the ability to be trapped at local minima. The optimization difficulties are resolved by combining both optimization techniques, thus forming TLBO-HHOA. TLBO-HHOA can give pseudo-optimal solutions to the optimization problem.

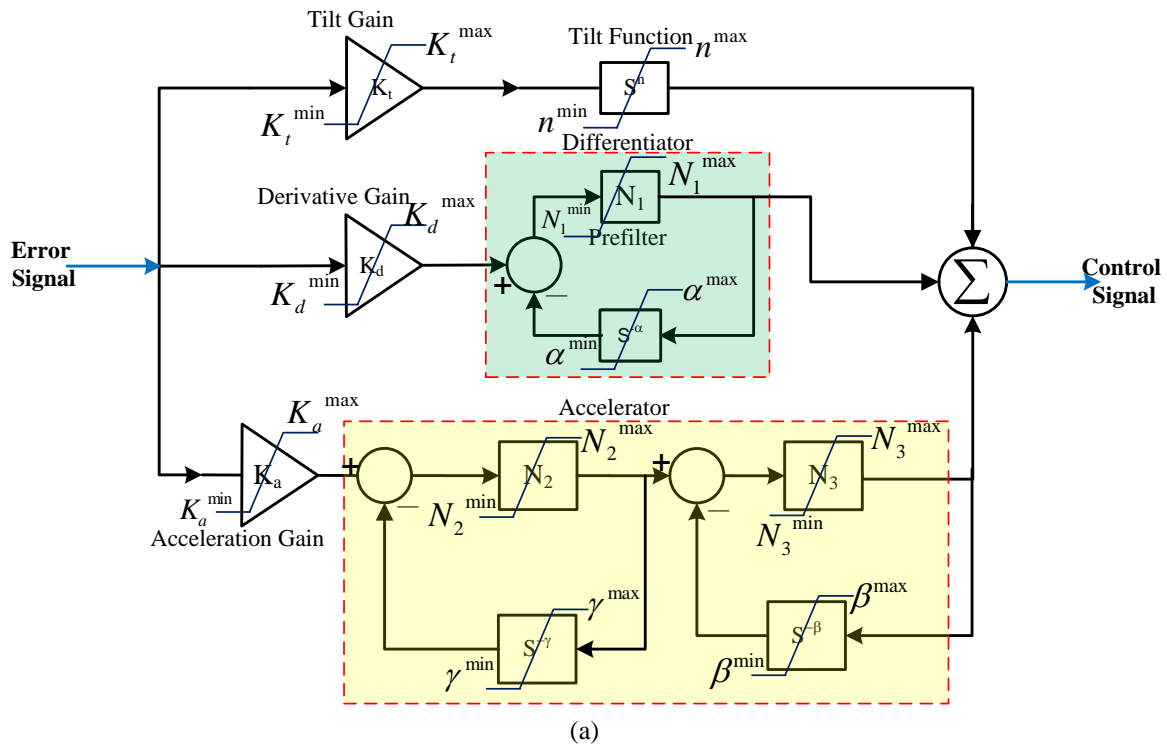
The optimization algorithm parameters are presented in Table 5. The values of optimization algorithm parameters are chosen such that the optimized values of control parameters are achieved quickly. The optimization is carried out till the stopping criterion (maximum iteration) is reached. Based on the lowest value of ITAE, the optimal values of control parameters are selected. The optimized values of control parameters along with their limits are presented in Table 6. The lower and upper bounds of the control parameters are obtained by performing optimization individually by both methods. The block diagram of the TLBO-HHOA regulated FOTDAF control technique is shown in Figure 4(a). The working principle of HTLB-HHOA is clearly described with the aid of a flowchart represented in Figure 4(b).

Table 5. Optimization parameters for TLBO-HHOA.

Criteria	Values	Criteria	Values
Population size	50	Defense of β horses	0.20
Maximum number of iterations	1000	Grazing of γ horses	1.50
Reduction factor	0.95	Hierarchy of γ horses	0.50
Percentage of best horses	0.15	Sociability of γ horses	0.10
Percentage of worst horses	0.25	Imitation of γ horses	0.30
Grazing of α horses	1.50	Defense of γ horses	0.10
Defense of α horses	0.50	Roaming of γ horses	0.05
Grazing of β horses	1.50	Grazing of δ horses	1.50
Hierarchy of β horses	0.90	Roaming of δ horses	0.10
Sociability of β horses			0.20

Table 6. TLBO-HHOA regulated FOTDAF optimized parameter values.

Parameter	Indices Name	Lower Limit	Indices Name	Upper Limit	Optimized Values
K_t	K_t^{min}	0.2692	K_t^{max}	0.538	0.2791
K_a	K_a^{min}	0.2174	K_a^{max}	0.3812	0.3333
K_d	K_d^{min}	0.3801	K_d^{max}	0.6462	0.4945
n	n^{min}	0.2712	n^{max}	0.70712	0.5054
α	α^{min}	0.6192	α^{max}	0.8462	0.7174
β	β^{min}	0.1082	β^{max}	0.594	0.4055
γ	γ^{min}	0.14	γ^{max}	0.3319	0.2311
N_1	N_1^{min}	68.654	N_1^{max}	225.659	123.8861
N_2	N_2^{min}	44.68	N_2^{max}	189.678	99.87
N_3	N_3^{min}	234.648	N_3^{max}	296.38	271.12



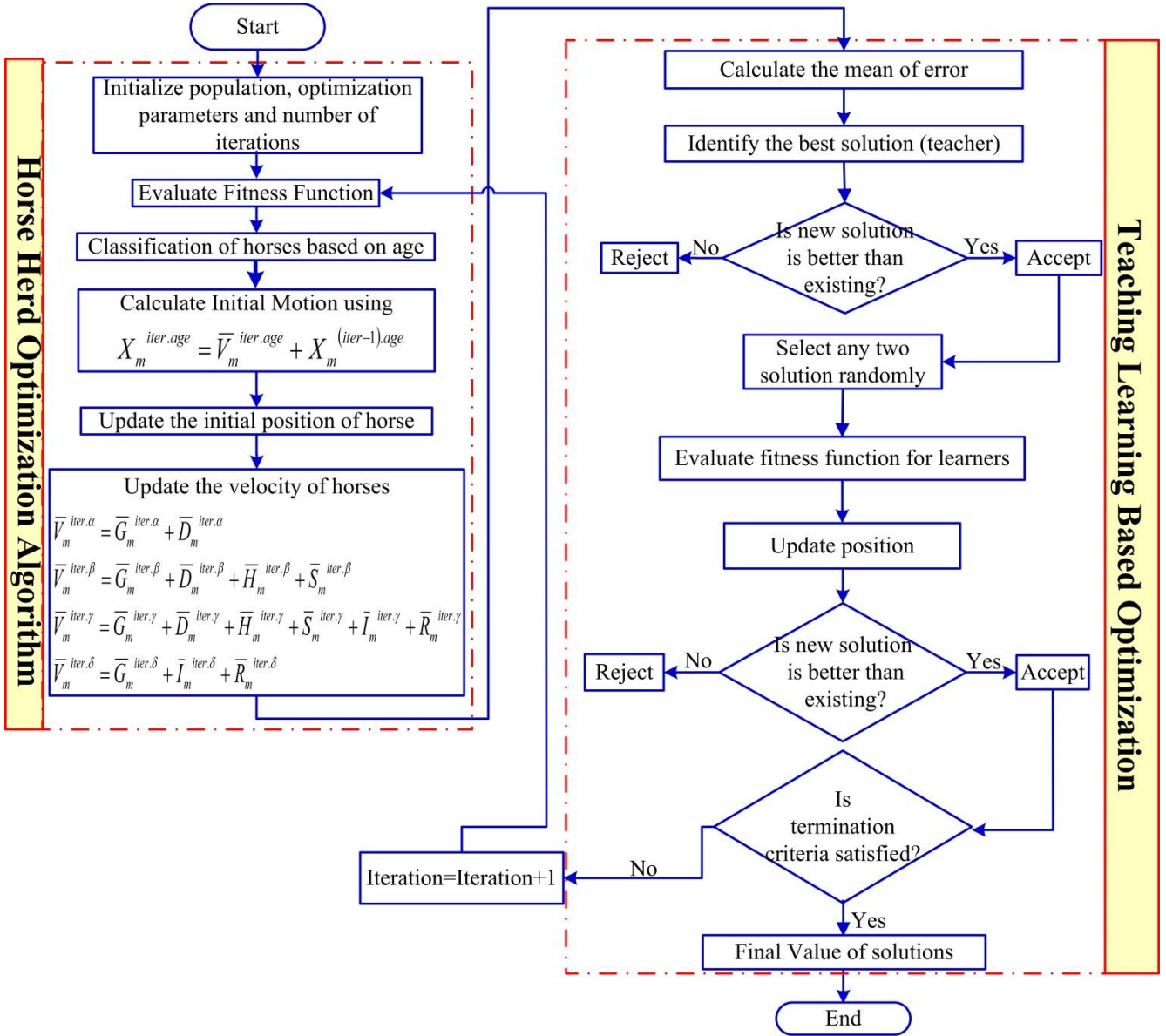


Figure 4. (a) Block Diagram of TLBO-HHOA regulated FOTDAF; (b) Flowchart of TLBO-HHOA.

3.3. Disturbance rejection analysis

Reference to Disturbance Ratio (RDR) is employed to perform disturbance rejection analysis of the TLBO-HHOA regulated FOTDAF controller (Tufenkci et al., 2020). The ratio between energies of the reference signal and disturbance signal is premeditated through RDR analysis. When $RDR \gg 1$, the control technique exhibits efficient disturbance rejection. Conversely, if $RDR \ll 1$, then the technique fails to exhibit disturbance rejection properties. A high value of RDR can be maintained by increasing the transmissibility from system input to plant input and reducing the transmissibility from disturbance input to plant input. The robustness of the TLBO-HHOA-regulated FOTDAF controller is improved when the RDR value is listed in the control design problem. The RDR is expressed mathematically in db by Equation (63).

$$RDR = 10 \times \log_{10} \left(\left(\sqrt{C(j\omega)_{real}^2 + C(j\omega)_{imag}^2} \right)^2 \right) \quad (63)$$

where $C(j\omega)_{real}$ and $C(j\omega)_{imag}$ are real and imaginary coefficients of the controller transfer function. $C(j\omega)_{real}$ and $C(j\omega)_{imag}$ values for the TLBO-HHOA-regulated FOTDAF controller are expressed mathematically by Equations (64 & 65), respectively.

$$C(j\omega)_{real} = \left[\begin{aligned} & K_t \omega^{-n} \cos \frac{n\pi}{2} + \frac{K_d N_3 \omega^\gamma}{N_3^2 + \omega^{2\gamma}} + \frac{K_d N_3^2 \omega^\gamma}{N_3^2 + \omega^{2\gamma}} \cos \frac{\pi\gamma}{2} \\ & + \frac{K_d N_1^2 N_2 \omega^{(\alpha+\beta)}}{(N_1^2 + \omega^{2\alpha})(N_2^2 + \omega^{2\beta})} \cos \frac{\pi(\alpha+\beta)}{2} \\ & - \frac{K_d N_1^2 N_2 \omega^{(\alpha+2\beta)}}{(N_1^2 + \omega^{2\alpha})(N_2^2 + \omega^{2\beta})} \cos \frac{\pi(\alpha+2\beta)}{2} \\ & + \frac{K_d N_1 N_2^2 \omega^{(2\alpha+\beta)}}{(N_1^2 + \omega^{2\alpha})(N_2^2 + \omega^{2\beta})} \cos \frac{\pi(2\alpha+\beta)}{2} \\ & + \frac{K_d N_1 N_2 \omega^{2(\alpha+\beta)}}{(N_1^2 + \omega^{2\alpha})(N_2^2 + \omega^{2\beta})} \cos \frac{\pi 2(\alpha+\beta)}{2} \end{aligned} \right] \quad (64)$$

$$C(j\omega)_{imag} = \begin{bmatrix} -K_t \omega^{-n} \sin \frac{n\pi}{2} + \frac{K_a N_3^2 \omega^\gamma}{N_3^2 + \omega^{2\gamma}} \sin \frac{\pi\gamma}{2} \\ - \frac{K_a N_1^2 N_2 \omega^{(\alpha+\beta)}}{(N_1^2 + \omega^{2\alpha})(N_2^2 + \omega^{2\beta})} \sin \frac{\pi(\alpha+\beta)}{2} \\ - \frac{K_a N_1^2 N_2 \omega^{(\alpha+2\beta)}}{(N_1^2 + \omega^{2\alpha})(N_2^2 + \omega^{2\beta})} \sin \frac{\pi(\alpha+2\beta)}{2} \\ + \frac{K_a N_1 N_2^2 \omega^{(2\alpha+\beta)}}{(N_1^2 + \omega^{2\alpha})(N_2^2 + \omega^{2\beta})} \sin \frac{\pi(2\alpha+\beta)}{2} \\ + \frac{K_a N_1 N_2 \omega^{2(\alpha+\beta)}}{(N_1^2 + \omega^{2\alpha})(N_2^2 + \omega^{2\beta})} \sin \frac{\pi 2(\alpha+\beta)}{2} \end{bmatrix} \quad (65)$$

The power spectral density of the transfer function of the TLBO-HHOA-regulated FOTDAF controller gives information about the ability of disturbance suppression. This indicates that the disturbance rejection capability depends on the control structure. Therefore, disturbance rejection analysis is a control structure design problem. The RDR plot of the proposed control technique is represented in Figure 5. It is evident from Figure 5 that the RDR value is 102.43. The disturbance rejection ability of the HTLB-WOA-regulated VPFOTADF controller is adequate.

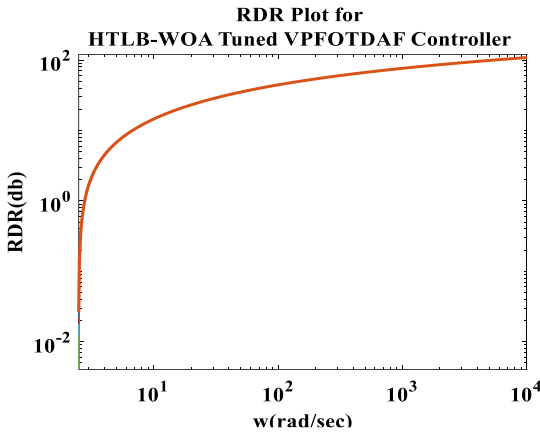


Figure 5. RDR plot for the TLBO-HHOA-regulated FOTDAF controller.

3.4. Sensitivity analysis of TLBO-HHOA-regulated FOTDAF

The settings of the controller affect the system performance. Hence, the proper setting of control parameters is crucial [16]. In the optimization technique, the fitness function is used to optimize control parameters, but it does not optimize the response itself. When control parameters are treated as constants, the controllers often exhibit poor robustness and maximize rise time. To achieve optimization in terms of response or robustness, control parameters are allowed to vary based on the error. The error signal ($f(e)$) can be expressed mathematically by Equation (66).

$$f(e) = \frac{\sqrt{2}}{\sqrt{\pi}} \int_0^t \left| e^{-\frac{t^2}{2}} \right| dt \quad (66)$$

The TLBO-HHOA-regulated FOTDAF is modeled to incorporate variations in control parameters. This variation in control parameters aims to improve the disturbance rejection ability, achieve a faster system response, and reduce overlapping. The upper and lower ranges of control parameters are placed in Table 4. The use of tilt gain enables rapid response with reduced settling time, but improper tuning can lead to increased system oscillations. The parametric variation of the tilt gain is plotted in Figure 6 (a). A decrease in the magnitude of steady-state error is achieved using

acceleration, coefficient of tilt, and derivative gain. However, improper margins tend to induce rapid oscillations and overshoot. The acceleration, coefficient of tilt, and derivative gain parameter variations are plotted in Figure 6 (a). The coefficient of acceleration and derivative facilitate proper controller tuning and disturbance rejection. The variation in the coefficient of acceleration and derivative is plotted in Figure 6 (b). The disturbance present in the response of the TLBO-HHOA-regulated FOTDAF controller is achieved by the use of a low-pass filter. The low-pass filter is implemented by using prefilter gains (N_1, N_2 , and N_3). The parametric variation of prefilter gains (N_1, N_2 and N_3) is presented in Figure 6 (c). The variation V_b is presented in Figure 6 (d). The variation in V_b is 0.22 volts, which is 0.44%.

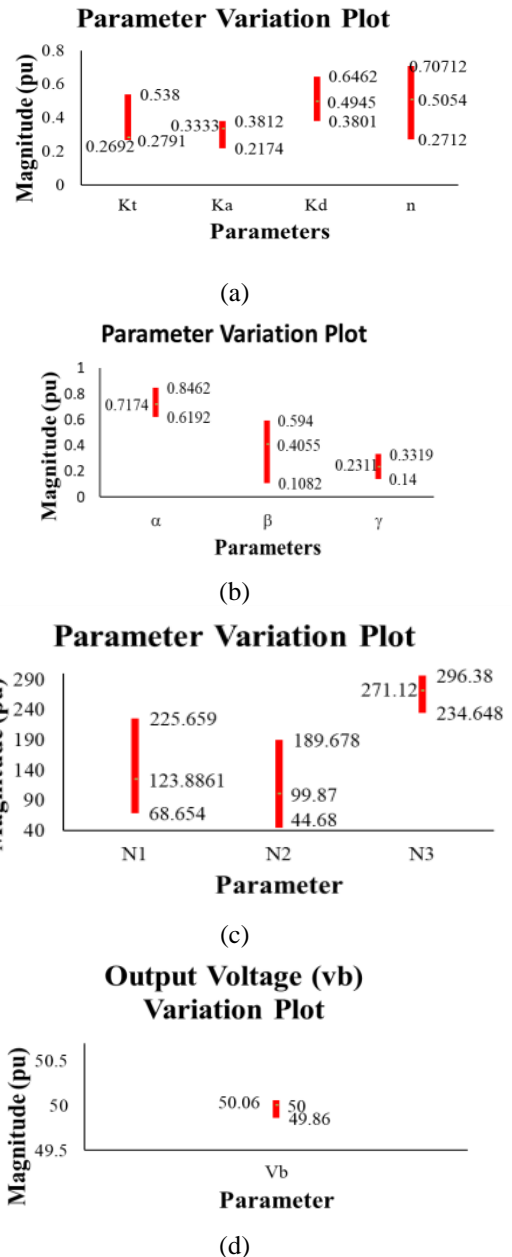


Figure 6.(a) The variation of K_t, K_a, K_d and n (b) The variation of α, β , and γ ; (c) The variation of N_1, N_2 and N_3 ; (d) The variation of V_b with variation in control parameters.

The step response of the proposed control technique is validated by performing the step response analysis of the proposed controller with other established control techniques

like Fuzzy+PID, FOTID, and PID controllers. Figure 7 (a) shows clearly that the FOTDAF controller has the best response among other controllers. RDR analysis provides another measure for the improved performance of the proposed control technique. From Figure 7 (b), it is clear that the FOTDAF controller has a superior noise rejection ability compared to other well-established control techniques.

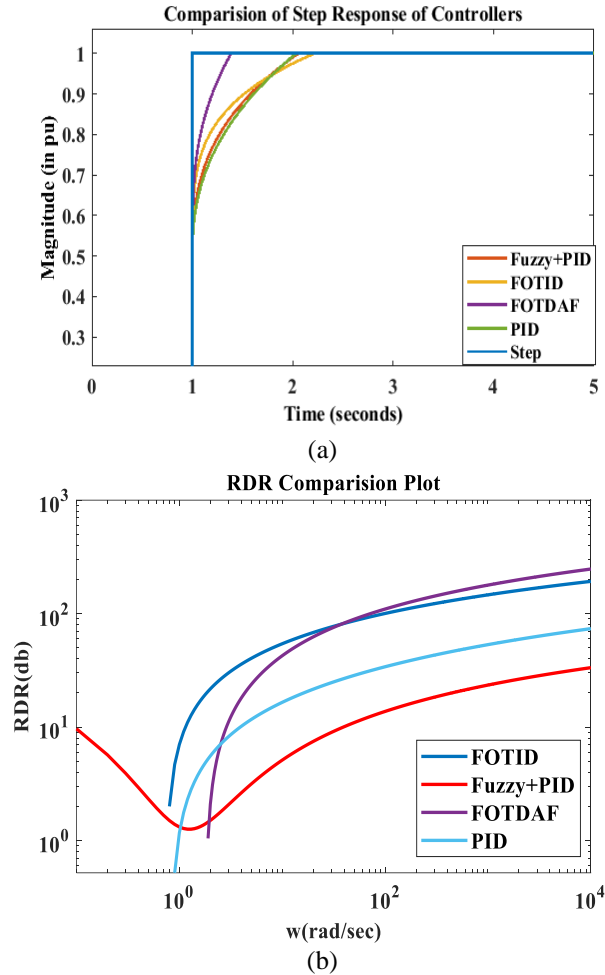


Figure 7. (a) Step response comparison of FOTDAF controller with other established control techniques; (b) RDR Comparison of FOTDAF controller with other established control techniques.

4. RESULTS AND DISCUSSIONS

The objective of this section is to analyze the output of the TLBO-HHOA regulated FOTDAF-based photovoltaic model and provide evidence of the superior performance, robustness, and stability achieved by the proposed strategy. The analysis aims to showcase the improvements in control action implemented in the proposed photovoltaic system.

4.1. Closed-loop IFOBC

The low voltage from solar panels lacks direct utilization. Thus, necessary measures need to be in place to heighten the magnitude of the solar panels. This enhancement is achieved by the use of an IFOBC. The switches in the IFOBC are switched at 370 KHz by the FOTDAF controller. Figure 8 represents the output voltage from the IFOBC. In low-rating converters, the average value of output voltage is 48 volts. For low-rating converters, 50 volts is a

serious output. Thus, for enhanced performance, the relift converter is designed to give an output voltage of 50 volts.

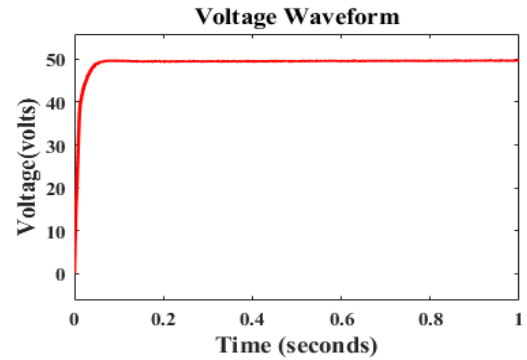


Figure 8. DC voltage output of IFOBC.

4.2. Closed-loop RSMI

When fed to 15-level RSMI, V_b gets inverted to AC. The magnitude V_{inv} is 220 volts. Figure 9 represents the plot for the output voltage of the 15-level RSMI. The 15-level RSMI is connected to an impedance of $100+240e^{-3j} \Omega$. The magnitude I_{inv} is 2 Ampere. Figure 10 represents the plot for the output current of the 15-level RSMI. P_{inv} is 360 watts and depicted in Figure 11.

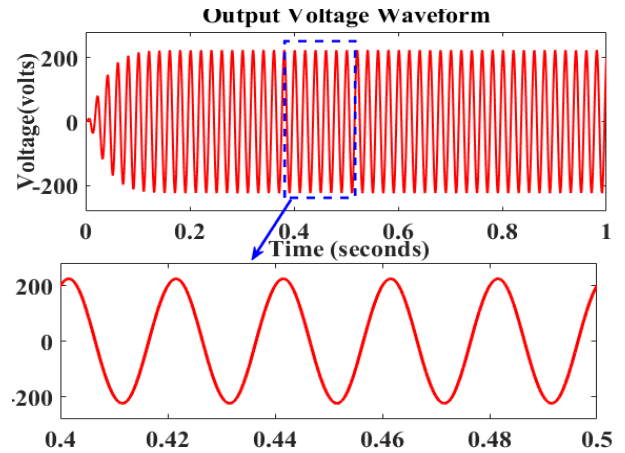


Figure 9. Output voltage of RSMI.

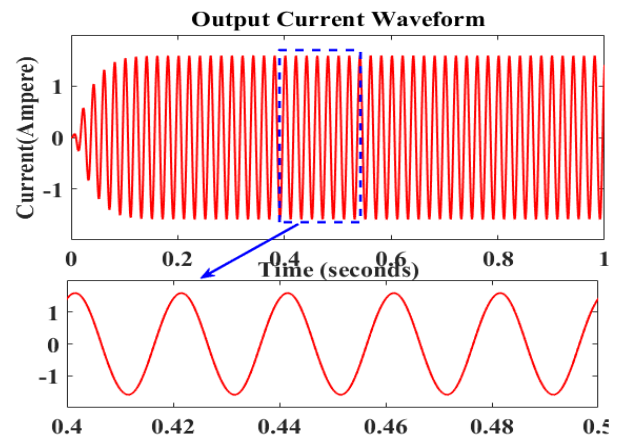


Figure 10. Output current of RSMI.

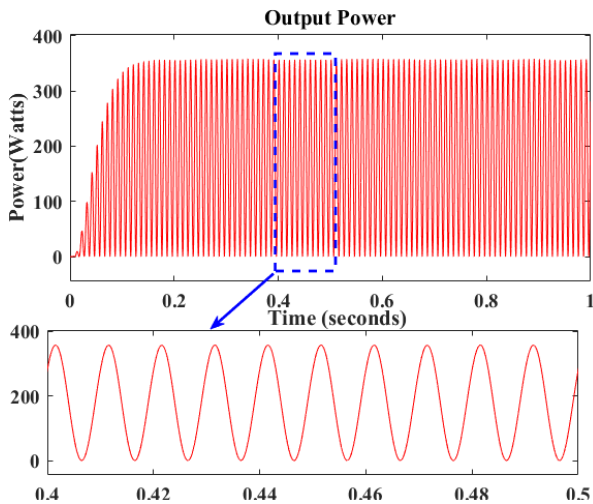
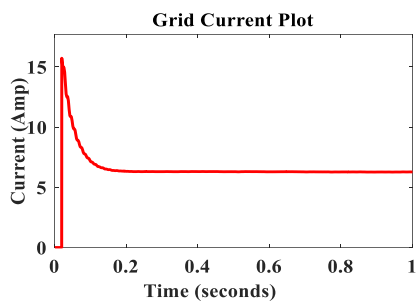
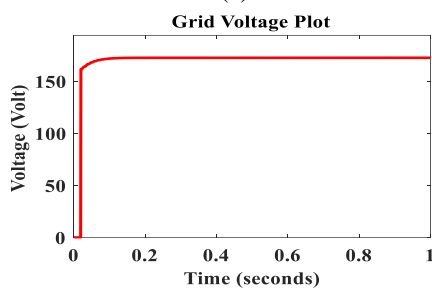


Figure 11. Output power of RSMI.

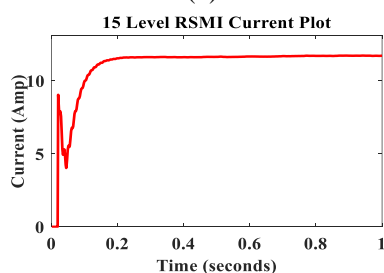
The load of 12KW is fed by both 15-level RSMI and grid. Both grid and 15-level RSMI are connected to the load and are capable of supplying the load in the standalone mode. Figure 12 represents the energy supplied and consumption pattern for the load. The load takes a voltage of 162.5 volts (RMS) from both the 15-level RSMI and grid while drawing a current of 6.3 amperes from the grid and 11.63 amperes from the 15-level RSMI. The voltage supplied by the grid and 15-level RSMI is represented in Figure 12(d, e). The current supplied by the grid and 15-level RSMI is represented in Figure 12(a, b). The load operates at a voltage of 169.5 volts and a current of 8.134 amperes. It is represented in Figure 12(c, f).



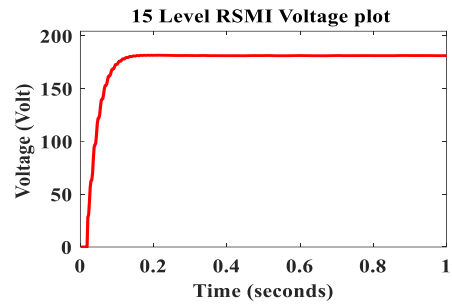
(a)



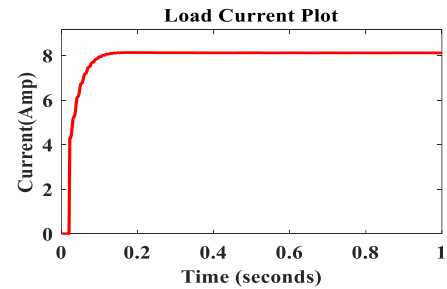
(b)



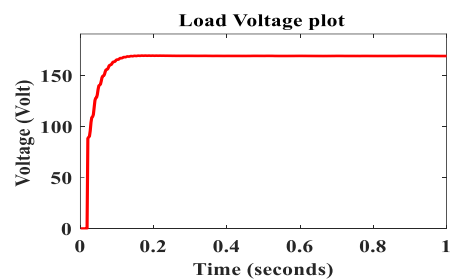
(c)



(d)



(e)



(f)

Figure 12.(a) Current supplied by the grid; (b) Voltage supplied by the grid; (c) Current supplied by RSMI; (d) Voltage supplied by RSMI; (e) Load current plot; (f) load voltage plot.

4.3. Real-time simulations

RT Lab (RTL) allows the end users to simulate the Simulink model in its real-time simulation platform. RTL handles synchronization and user interface for seamless distributed execution. In this study, the performance of the proposed photovoltaic system was tested using the OPAL-RT simulator OP4510, which is software in the loop-based real-time simulator. The modeling and simulation of the proposed photovoltaic system are synchronized to the OPAL-RT simulator OP4510 using real-time software, which interfaces with the sensing board, host computer, OPAL-RT simulator OP4510 configurable board, and Field Programmable Gate Array (FPGA) Xilinx Kintex7 325T synchronization to a real-time lab by using OPAL-RT simulator OP4510. The real-time setup of OPAL-RT is placed in Figure 13.

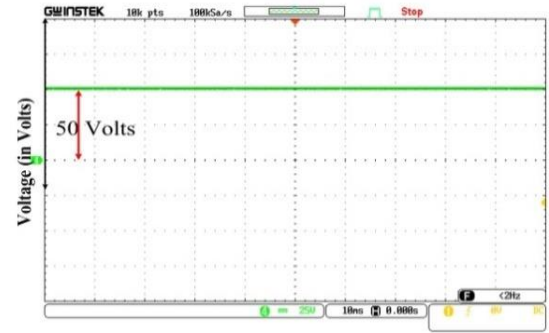


Figure 13. Real-time setup of OPAL-RT.

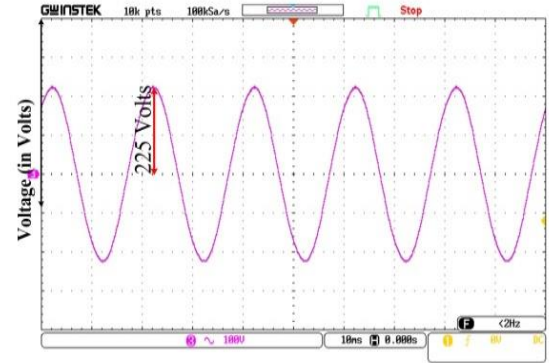
The detailed parameters of the proposed PV system are placed in Table 7. The output voltage for the IFOBC is placed in Figure 14 (a). The output voltage, current, and power for the 15-level RSMI are represented in Figure 14 (b-d), respectively.

Table 7. Specification and parameter of the proposed PV system.

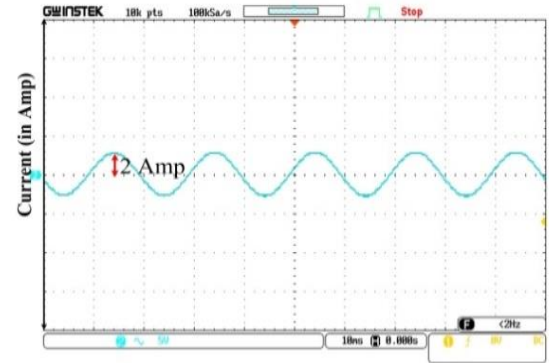
Maximum power	60 watt	
Voltage at maximum power	33.54 volts	
Current at maximum power	1.89 ampere	
Open-circuit voltage	39.66 volts	
Short-circuit current	1.99 ampere	
IFOBC Inductor (L_{in})	0.0931 mH	
Solar panel resistance (R_{SP})	7 Ω	
IFOBC input voltage (V_j)	22 volts	
IFOBC output voltage (V_b)	50 volts	
IFOBC output resistance (R_L)	50 Ω	
IFOBC output capacitor (C_{out})	400 μ F	
Equivalent series resistance of inductor (R_{in})	≤ 1 Ω	
Equivalent series resistance of inductor (R_{Co})	≤ 1 Ω	
Diode	Maximum reverse voltage	100 volts
	Maximum forward current	40 ampere
	Forward bias voltage	0.8 volts
	Resistance of diode (R_{Diode})	1 m Ω
IGBT	Maximum collector current	30 ampere
	Collector emitter voltage (saturation)	1.95 volts
	Maximum collector emitter voltage	650 volts
	Resistance of IGBT (R_{ONIGBT})	1 m Ω
Switching frequency (f_s)	8,500 Hz	
Duty cycle (D)	0.1458	
Diode	Maximum reverse voltage	100 volts
	Maximum forward current	40 ampere
	Forward bias voltage	0.8 volts
	Resistance of diode (R_{Diode})	1 m Ω
IGBT	Maximum collector current	30 ampere
	Collector emitter voltage (saturation)	1.95 volts
	Maximum collector emitter voltage	650 volts
	Resistance of IGBT (R_{ONIGBT})	1 m Ω



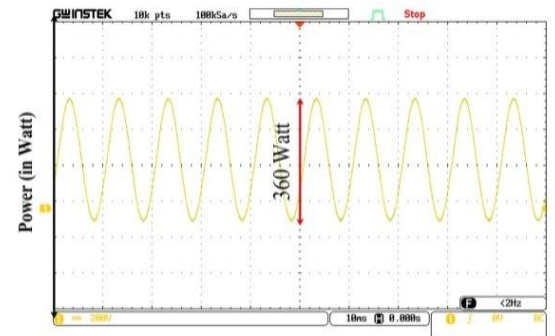
(a)



(b)



(c)



(d)

Figure 14. Real-time simulation plot for (a) Output voltage of IFOBC; (b) Output voltage of 15-level RSMI; (c) Output current of 15-level RSMI; (d) Output power of 15-level RSMI.

4.4. Robustness analysis

The ability to endure a rapid or abnormal change in operating conditions is called the robustness of the system. The operating conditions of the proposed photovoltaic system are irradiance and temperature. The robustness is verified if the change in operating conditions does not impact the system

responses. The robustness of the proposed photovoltaic system is analyzed for changes in voltage, current, and power of the 15-level RSMI. The optimal operating range of temperature for photovoltaic activity is from 20 °C to 48 °C. The deviations in RMS value ranging from 160.98 volts to 161.24 volts are represented in Figure 15(a). This deviation of 0.26 volts amounts to a 0.162% variation from the full load. The deviation in output current from the 15-level RSMI is between 1.4125 amp and 1.4135 ampere. This deviation in the current of 0.001 amp amounts to 0.074% variation from the full load, as represented in Figure 15 (b). The variation in output power of 15-level RSMI at full load is 0.645%, which is represented in Figure 15 (c). It is seen to vary between 248.3 watts and 294.8 watts. The power per unit area is received from the sun on a horizontal surface at sea level. The maximum value of irradiance is 1361 watts/square meter (W/M^2). The variation in irradiance is from 700 W/M^2 to 1361 W/M^2 . The irradiance range is chosen as it represents the optimal range for the generation of voltage from photovoltaic panels. The output voltage of 15-level RSMI varies between 160.98 volts and 164.5 volts, as depicted in Figure 15 (d). This variation of 3.52 volts is 2.18% from the full load. Figure 15(e) represents the variation of current from 15-level RSMI. This variation in the 15-level RSMI output current is 0.003 amp (1.4125 amp to 1.4155 amp), which is 0.022% of full load current. The deviations in power are 10 watts (245 watts to 255 watts). The 4.03% deviation in output power of 15-level RSMI is represented in Figure 15(f). The proposed system witnessed minute variations (within the tolerance level of 5%) under large-scale fluctuations in operating conditions. The PV system is not prone to disturbances, thereby exhibiting robust characteristics.

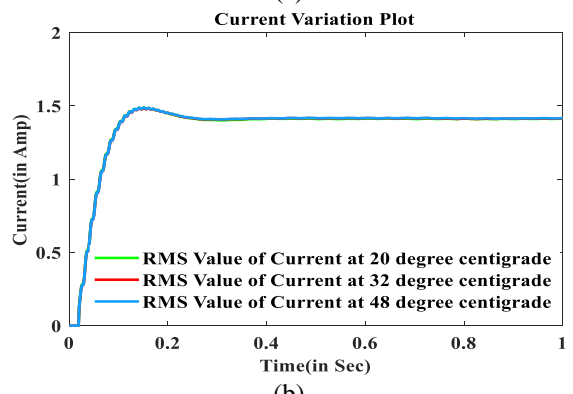
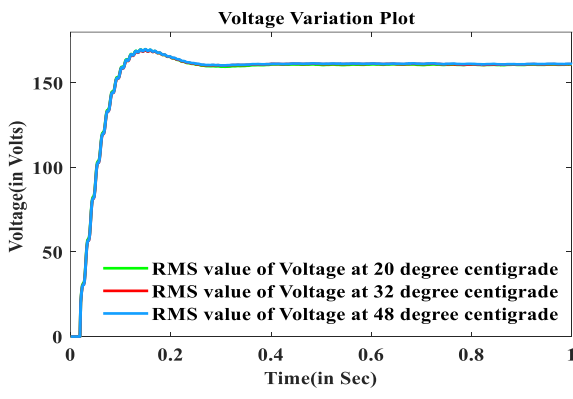
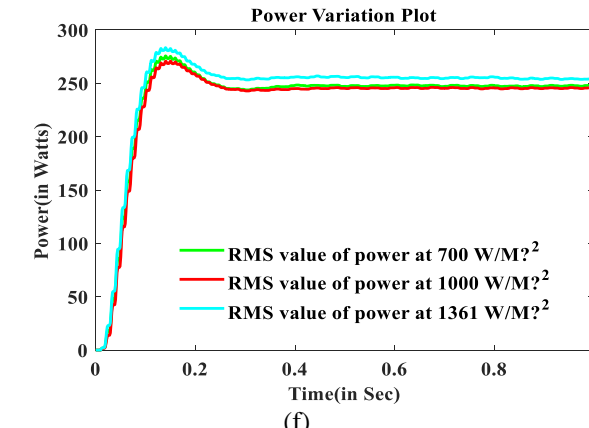
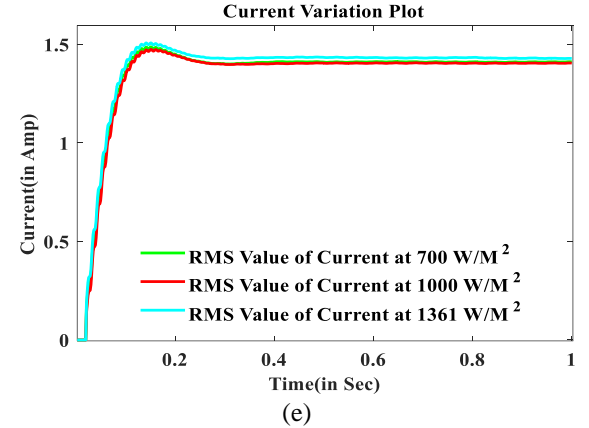
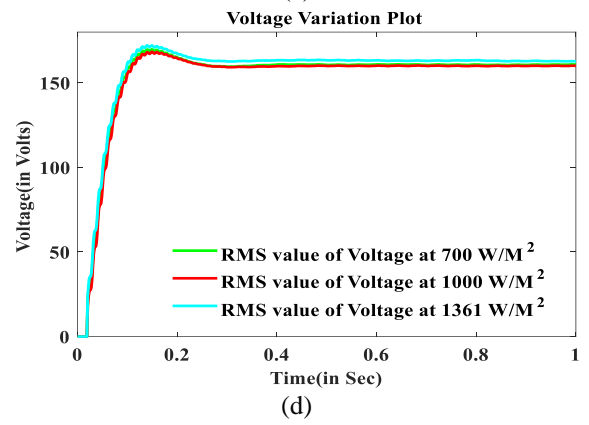
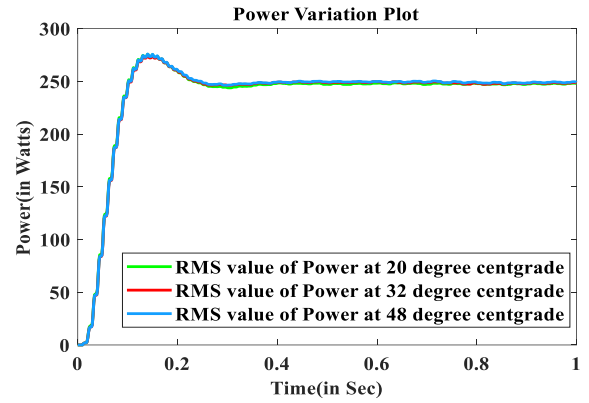


Figure 15. (a) Variation of V_{inv} with temperature variation; (b) Variation of I_{inv} with temperature variation; (c) Variation of P_{inv} with temperature variation; (d) Variation of V_{inv} with variation in irradiance; (e) Variation of I_{inv} with variation in irradiance; (f) Variation of P_{inv} with variation in irradiance.

5. CONCLUSION

Within the purview of this manuscript, a grid-connected photovoltaic system was implemented. The photovoltaic system consisted of IFOBC, TLBO-HHOA-regulated FOTDAF, RSMI, and SVPWM. The suggested control strategy, when implemented, improved the robustness and stability and reduced harmonic distortions. The utilization of a fractional-order controller along with the SVPWM technique improved the stability, robustness, and harmonic rejection capability of the photovoltaic system. Moreover, the utilization of the FOTDAF controller improved stability besides improving disturbance rejection ability. The proposed photovoltaic system experienced fewer fluctuations when subjected to variations in input parameters. The simulated results served for justification purposes. The results demonstrated the effectiveness of the control technique towards more reliable operation as compared to avant-garde control techniques. The superior performance, robustness, and stability of TLBO-HHOA regulated FOTDAF together with the SVPWM technique were realized and the presented results authenticated its hardware implementation.

CONTRIBUTORSHIP

All the authors have contributed equally to the design and implementation of the research, the analysis of the results, and the writing of the manuscript.

FUNDING

The authors declare that they have not received any funding from any organization that could have appeared to influence the work reported in this paper.

ACKNOWLEDGEMENT

The authors would like to acknowledge and appreciate Siksha 'O' Anusandhan University for their support. This research received no funding.

REFERENCES

- Alluhaybi, K., Batarseh, I. & Hu, H. (2019). Comprehensive review and comparison of single-phase grid-tied photovoltaic microinverters *IEEE Journal of Emerging & Selected Topics in Power Electronics*, 8(2), 1310-1329. <https://doi.org/10.1109/JESTPE.2019.2900413>.
- Ayop, R. & Tan, C.W. (2018). Design of boost converter based on maximum power point resistance for photovoltaic applications. *Solar Energy*, 160(1), 322-335. <https://doi.org/10.1016/j.solener.2017.12.016>.
- Darmawardana, D., Perera, S., Meyer, J., Robinson, D., Jayatunga, U. & Elphick, S. (2019). Development of high frequency (Supraharmonic) models of small-scale (< 5 kW), single-phase, grid-tied PV inverters based on laboratory experiments. *Electric Power Systems Research*, 177(1), p.105990. <https://doi.org/10.1016/j.epsr.2019.105990>.
- Eberlein, S. & Krzysztof, R. (2021). Small-signal stability modeling, sensitivity analysis & optimization of droop controlled inverters in LV microgrids. *International Journal of Electrical Power & Energy Systems*, 125(1), 106404. <https://doi.org/10.1016/j.ijepes.2020.106404>.
- Eker, E. & Ekinci, S. (2021). A new fusion of ASO with SA algorithm & its applications to MLP training & DC motor speed control. *Arabian Journal for Science & Engineering*, 46(4), 3889-3911. <https://doi.org/10.1007/s13369-020-05228-5>.
- Fahad, M. & Ekhilef, S. (2021). Implementation & analysis of a 15-level inverter topology with reduced switch count. *IEEE Access*, 9 (1), 40623-40634. <https://doi.org/10.1109/ACCESS.2021.3064982>.
- Fang, S., & Wang, X. (2020). Modeling & analysis method of fractional-order buck-boost converter. *International Journal of Circuit Theory & Applications*, 48(9), 1493-1510. <https://doi.org/10.1002/cta.2840>.
- Fani, B., Moazzami, M. & Farhoodi, E. (2019). Harmonic Voltage Reduction by using Droop Controller in Inverters Parallel Operation. *Iranian Journal of Electrical & Computer Engineering*, 71(2), p.97. <https://dori.net/dor/20.1001.1.16823745.1398.17.2.2.7>.
- Guohua, L., & Feng, L. (2022). Single-Phase Voltage Source Multi-Level Inverter Hysteresis SVPWM Reconfigurable Fault-Tolerant Control Method. *Energies*, 15(7), 2557. <https://doi.org/10.3390/en15072557>.
- Izci, D. & Ekinci, S. (2022). A Novel Hybrid ASO-NM Algorithm & Its Application to Automobile Cruise Control System. In *Proceedings of 2nd International Conference on Artificial Intelligence: Advances & Applications*, Springer, Singapore) 333-343. https://doi.org/10.1007/978-981-16-6332-1_29.
- Izci, D. & Ekinci, S. (2022). A novel improved arithmetic optimization algorithm for optimal design of PID controlled & Bode's ideal transfer function based automobile cruise control system. *Evolving Systems*, 13(3), 453-468. https://doi.org/10.1007/978-981-16-6332-1_29.
- Izci, D. & Hekimoğlu, B. (2022). Fractional-order PID controller design for buck converter system via hybrid Lévy flight distribution & simulated annealing algorithm. *Arabian Journal for Science & Engineering*, 47(11), 13729-13747. <https://doi.org/10.1007/s13369-021-06383-z>.
- Jia, Z. & Liu, C. (2018). Fractional-order modeling & simulation of magnetic coupled boost converter in continuous conduction mode. *International Journal of Bifurcation & Chaos*, 28(5), 1-25. <https://doi.org/10.1142/S021812741850061X>.
- Karimi, H., Shahgholian, G., Fani, B., Sadeghkhani, I. & Moazzami, M. (2019). A protection strategy for inverter-interfaced isl&ed microgrids with looped configuration. *Electrical Engineering*, 101(3), 1059-1073. <https://doi.org/10.1007/s00202-019-00841-6>.
- Keddar, M. & Midoun, A. (2019). Interconnection performance analysis of single phase neural network based NPC & CHB multilevel inverters for grid-connected PV systems. *International Journal of Renewable Energy Research (IJRER)*, 9(3), 1451-1461. <https://doi.org/10.20508/ijrer.v9i3.9593.g7730>.
- Lakshmi, V. & Mohanaiah, P. (2021). WOA-TLBO: whale optimization algorithm with teaching-learning-based optimization for global optimization & facial emotion recognition. *Applied Soft Computing*, 110(1), 107623. <https://doi.org/10.1016/j.asoc.2021.107623>.
- Lin, H., & He, X. (2020). A Simplified 3-D NLM-Based SVPWM Technique With Voltage-Balancing Capability for 3LNPC Cascaded Multilevel Converter, *IEEE Transactions on Power Electronics*, 35(4), 3506-3518. <https://doi.org/10.1109/TPEL.2019.2938606>.
- Liu, B., Zhang, Z., Li, G., He, D., Chen, Y., Zhang, Z., Li, G. & Song, S. (2022). Integration of power decoupling buffer & grid-tied photovoltaic inverter with single-inductor dual-buck topology & single-loop direct input current ripple control method. *International Journal of Electrical Power & Energy Systems*, 125(1), p.106423. <https://doi.org/10.1016/j.ijepes.2020.106423>.
- Logeswaran, T., & Karuppusamy, P. (2015). Adaptive neuro-fuzzy model for grid-connected photovoltaic system. *International Journal of Fuzzy Systems*, 17(4), 585-594. <https://doi.org/10.1007/s40815-015-0078-4>.
- Marrero, L. & González, V.J. (2022). Harmonic distortion characterization in groups of distribution networks applying the IEEE St&ard 519-2014. *IEEE Latin America Transactions*, 19(4), 526-533. <https://doi.org/10.1109/TLA.2021.9448534>.
- Nguyen, P.C. & Nguyen, D.T. (2022). A new decentralized space vector PWM method for multilevel single-phase full bridge converters. *Energies*, 15(3), 1010. <https://doi.org/10.3390/en15031010>.
- Palanisamy, R., & Vijayakumar, V. (2020). Artificial neural network based SVPWM for five level cascaded H-bridge inverter fed grid connected PV system. *Journal of Intelligent & Fuzzy Systems*, 39(6), 8453-8462. <https://doi.org/10.3233/JIFS-189163>.

23. Patra, A. K. & Rout, P. K. (2020). Design of artificial pancreas based on the SMGC & self-tuning PI control in type-I diabetic patient. *International Journal of Biomedical Engineering & Technology*, 32 (1), 1-35. <https://doi.org/10.1504/IJBET.2020.104675>.
24. Patra, A. K. & N&a, A. (2021). Implantable Insulin Delivery System Based on the Genetic Algorithm PI Controller (GA-PIC). In *Advances in Intelligent Computing & Communication*, Springer, Singapore) 243-252. https://doi.org/10.1007/978-981-16-0695-3_24.
25. Rath, D., & Kar, S. (2021). Harmonic distortion assessment in the single-phase photovoltaic (PV) system based on spwm technique. *Arabian Journal for Science & Engineering*, 46(10), 9601-9615. <https://doi.org/10.1007/s13369-021-05437-6>.
26. Sampaio, L.P., Costa, P.J.S. & da Silva, S.A.O. (2022). Modified zeta inverter intended for single-phase grid-tied photovoltaic system. *Sustainable Energy Technologies & Assessments*, 52(1), p.102076. <https://doi.org/10.1016/j.seta.2022.102076>.
27. Sattianadan, D., & Gorai, S. (2020). Potency of PR controller for multiple harmonic compensation for a single-phase grid connected system. *International Journal of Power Electronics & Drive Systems*, 11(3), 1491-1498. <https://doi.org/10.11591/ijpeds.v11.i3.pp1491-1498>.
28. Siddique, M.D. & Memon, M.A. (2019). A new multilevel inverter topology with reduce switch count. *IEEE Access*, 7(1), 58584-58594. <https://doi.org/10.1109/ACCESS.2019.2914430>.
29. Tufenkci, S. & Matusu, R. (2020). Disturbance rejection FOPID controller design in v-domain. *Journal of Advanced Research*, 25 (1), 171-180.
30. Xie, L. & Zhang, B. (2020). A modeling & analysis method for CCM fractional order Buck-Boost converter by using R-L fractional definition. *Journal of Electrical Engineering & Technology*, 15(4), 1651-1661. <https://doi.org/10.1007/s42835-020-00426-5>.
31. Xu, J., & Xie, S. (2019). Harmonics & stability analysis of single-phase grid-connected inverters in distributed power generation systems considering phase-locked loop impact. *IEEE Transactions on Sustainable Energy*, 10(3), 1470-1480. <https://doi.org/10.1109/TSTE.2019.2893679>.
32. Yao, H., & Xia, C. (2021). A novel SVPWM scheme for field-oriented vector-controlled PMSM drive system fed by cascaded H-bridge inverter. *IEEE Transactions on Power Electronics*, 36(8), 8988-9000. <https://doi.org/10.1109/TPEL.2021.3054642>.
33. Yao, J. & Ma, Z. (2021). Advances in Modeling & Reduction of Conducted & Radiated EMI in Non-isolated Power Converters. *IEEE Applied Power Electronics Conference & Exposition (APEC)IEEE.*, 1-6, 9487164. <https://doi.org/10.1109/APEC42165.2021.9487164>.
34. Yusof, N.F.M., Ishak, D. & Salem, M. (2022). An Improved Control Strategy for Single-Phase Single-Stage Grid-Tied PV System Based on Incremental Conductance MPPT, Modified PQ Theory, & Hysteresis Current Control. *Engineering Proceedings*, 12(1), p.91. <https://doi.org/10.3390/engproc2021012091>.